Chemical Geology 690 (2025) 122885

Contents lists available at ScienceDirect

Chemical Geology

journal homepage: www.elsevier.com/locate/chemgeo

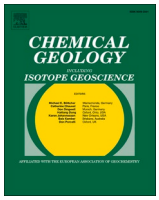

Early diagenetic versus hydrothermal signals in pyrite from ancient metamorphic sediment-hosted massive sulfides – implications for the stability of sulfur and iron isotope records in deep time

Eric Runge [a,b,*], Muammar Mansor [c], Virgil Pasquier [d], Thomas Bovay [d], Johanna Marin-Carbonne [d], Vanessa Fichtner [a], Andreas Kappler [c,e], Jan-Peter Duda [a,b]

[a] Department of Geobiology, Geoscience Center, University of Göttingen, Göttingen, Germany
[b] Sedimentology and Organic Geochemistry, Department of Geosciences, Tübingen University, Tübingen, Germany
[c] Geomicrobiology, Department of Geosciences, Tübingen University, Tübingen, Germany
[d] Institute of Earth Sciences, Université de Lausanne, Lausanne, Switzerland
[e] Cluster of Excellence EXC 2124, Controlling Microbes to Fight Infection, Tübingen University, Tübingen, Germany

ARTICLE INFO

Editor: Marco Fiorentini

Keywords:
Hydrothermal systems
SEDEX
Rammelsberg
SIMS
Mineral-fluid interaction

ABSTRACT

Stable isotope compositions in pyrite are widely employed for tracing microbial sulfur and iron cycling through geological time. In hydrothermal sulfide systems, however, sulfur and iron pools can be affected by both microbial and abiotic processes, limiting the applicability of the respective stable isotopes as biosignatures. Moreover, the diagenetic and metamorphic stability of sulfur and iron isotope signatures in pyrite under hydrothermal conditions is insufficiently understood. Here, we employed coupled in-situ Secondary Ion Mass Spectrometry (SIMS) triple sulfur ($\delta^{34}S$ and $\Delta^{33}S$) and iron ($\delta^{56}Fe$) isotope analysis on morphologically diverse pyrite in ~390 Ma sediment-hosted massive sulfides to better understand biosignature preservation in hydrothermal systems. Petrographic analysis reveals recrystallized or cemented framboid-like pyrite that was locally overgrown by a secondary generation of subhedral pyrite. $\delta^{34}S$ and $\Delta^{33}S$ signatures of the pyrites (−15.13 to +18.77 ‰ and − 0.21 to +0.26 ‰, respectively) can be explained by either microbial or thermochemical sulfate reduction. However, the isotopically lightest $\delta^{34}S$ value in framboid-like pyrite (−15.13 ‰) most likely represents a mixed signal of early diagenetic microbial sulfur cycling and later sulfidic hydrothermal fluids driving recrystallization or cementation. The same pyrites show highly variable $\delta^{56}Fe$ compositions (−1.30 to +2.19 ‰), indicating precipitation from hydrothermal Fe(II) at varying rates and/or pyritization of a diagenetically fractionated iron pool. The lower median $\delta^{56}Fe$ value in framboid-like versus subhedral pyrite points to a greater expression of kinetic and equilibrium fractionation in the former. This may reflect differences in precipitation rates between early diagenetic (microbial) processes and hydrothermal overprint of the system, consistent with textural evidence for framboid recrystallization or cementation, and overgrowth. Nevertheless, the likely presence of microbially formed pyrite and the incomplete equilibration with hydrothermal fluids highlight that signatures of early diagenetic redox cycling can be preserved in hydrothermal sulfides despite alteration by sulfidic fluids or greenschist metamorphism. Our study stresses the challenges and potentials of coupled textural and in-situ stable isotope analysis for tracing microbial sulfur and iron cycling in hydrothermal sulfide systems through Earth's history.

1. Introduction

Hydrothermal sulfide systems are among the most ancient habitats on Earth and, thus, may provide an essential window into the emergence and evolution of microbial metabolism (Rasmussen, 2000; Georgieva et al., 2021; Mißbach et al., 2021; Baumgartner et al., 2022; Runge et al., 2023a; Weimann et al., 2024). The ancient equivalents of these environments are volcanogenic and sediment-hosted massive sulfide deposits (Huston et al., 2010; Wilkinson, 2014; Tornos et al., 2015). In sedimentary systems, iron sulfide mineral formation (including pyrite,

* Corresponding author at: Department of Biology and Environmental Science, Linnaeus University, Kalmar, Sweden.
E-mail address: eric.runge@lnu.se (E. Runge).

https://doi.org/10.1016/j.chemgeo.2025.122885
Received 28 August 2024; Received in revised form 22 May 2025; Accepted 25 May 2025
Available online 26 May 2025

cubic FeS_2) is commonly mediated by microbial iron and sulfur cycling (Rickard, 1969; Strauss, 1997; Canfield et al., 1998; Donald and Southam, 1999; Picard et al., 2016; Thiel et al., 2019; Berg et al., 2020; Gorlas et al., 2022; Bronner et al., 2023; Truong et al., 2023; Runge et al., 2024; Smrzka et al., 2024). Since these processes can occur at temperatures exceeding 100 °C (e.g., Jørgensen et al., 1992; Kashefi and Lovley, 2003), some pyrite in hydrothermal environments may also derive from microbial sulfur and iron cycling. However, in these settings, pyrite commonly precipitates abiotically from iron-rich and sulfidic hydrothermal fluids (Schoonen and Barnes, 1991; Butler et al., 2004; Wang et al., 2022; Früh-Green et al., 2022) or may result from the abiotic sulfidation of magnetite (Canfield and Berner, 1987; Qian et al., 2010, 2013; Bendt et al., 2019; Runge et al., 2023b, 2024) at relatively high temperature. Thus, gleaning information on past microbial processes from ancient hydrothermal sulfides depends on our ability to distinguish biogenic from abiogenic pyrite, as well as primary pyrite from subsequent generations.

Major sulfur and iron stable isotopes (i.e., ^{32}S, ^{34}S, ^{54}Fe, ^{56}Fe) in pyrite are among the most applied tools for deciphering the biogenicity of pyrite in modern and ancient environments (Butler et al., 2004; Eickmann et al., 2014; Duda et al., 2016; Marin-Carbonne et al., 2020; Nozaki et al., 2020, 2024; Baumgartner et al., 2020; Pokrovski et al., 2021; Decraene et al., 2021; Moreras-Marti et al., 2022; Dupeyron et al., 2023; Reinhardt et al., 2024). In the case of stable sulfur isotopes, the largest fractionations are associated with microbial sulfur cycling (MSC) (Canfield, 2001). Dissimilatory sulfate reduction (DSR), possibly in conjunction with re-oxidation of sulfide and subsequent elemental sulfur disproportionation, can cause isotope fractionation approaching equilibrium ($\Delta^{34}S_{sulfate\text{-}sulfide} \approx 70$ ‰ at 20 °C: Sim et al., 2011a; Wing and Halevy, 2014; Halevy et al., 2023). Accordingly, strongly ^{34}S-depleted sulfide minerals in volcanogenic and sediment-hosted deposits throughout the geological record were interpreted as evidence for MSC (Eldridge et al., 1993; Taylor, 2004; Present et al., 2017; Lode et al., 2017; Slack et al., 2019; Velasco-Acebes et al., 2019).

The true fractionation during DSR can vary between 0 and 70 ‰, depending on the microbial strain and environmental parameters, such as carbon and sulfur availability or temperature (Chambers et al., 1975; Habicht et al., 2002; Farquhar et al., 2003; Bradley et al., 2016; Sim et al., 2023). At temperatures ≥100 °C, thermochemical sulfate reduction (TSR) dominates and can also cause substantial sulfur isotope fractionation via a kinetic isotope effect (KIE; maximum $\Delta^{34}S_{sulfate\text{-}pyrite} \approx 20$ ‰ at 100 °C: Kiyosu and Krouse, 1990; Machel et al., 1995). Theoretical estimates suggest that the equilibrium isotope effect (EIE) between sulfate and sulfide ($\Delta^{34}S_{sulfate\text{-}pyrite}$) at 100 °C is ≈ 43 ‰, giving an upper limit for sulfur isotope fractionation in TSR systems (Eldridge et al., 2016). Notably, Rayleigh distillation due to pyrite precipitation following DSR or TSR occurring under closed system conditions (i.e., when sulfate reduction rates exceed the resupply of sulfate) would produce ^{34}S-enriched sulfate in the residual porewater (Zaback et al., 1993; Jørgensen et al., 2004; Drake et al., 2018; Paiste et al., 2022). This can result in microscale $\delta^{34}S_{pyrite}$ values close to those of the initial sulfate source. Therefore, sulfide minerals in hydrothermal systems may not be ^{34}S-depleted even in the presence of DSR, suggesting biological activity remains undetected in many cases.

Minor sulfur isotopes (^{33}S and ^{36}S) might help disentangle microbial from abiotic sulfur cycling in hydrothermal deposits further. For instance, the theoretical relationship between the fractionation factors between sulfate and sulfide ($\alpha_{sulfate\text{-}sulfide} = R_{sulfate}/R_{sulfide}$; R = isotope ratio) for $^{33}S/^{32}S$ and $^{34}S/^{32}S$ ratios during mass-dependent equilibrium fractionation is related by the exponent $^{33}\theta$ and described by the function:

$$\alpha^{33/32}_{sulfate-sulfide} = \left(\alpha^{34/32}_{sulfate-sulfide}\right)^{^{33}\lambda}$$

However, the exponent $^{33}\lambda$ (0.515 at low-temperature equilibrium) varies slightly between different mass-dependent fractionation processes, resulting in deviations from the theoretical EIE expressed as non-zero $\Delta^{33}S$ (Farquhar et al., 2007). For instance, DSR, chemolithotrophic sulfide oxidation, and sulfur disproportionation are associated with $^{33}\theta$ between 0.5077 and 0.5187, corresponding to positive $\Delta^{33}S$ deviations in the produced sulfur species of up to ca. +0.23 ‰ (Johnston, 2005; Sim et al., 2011b; Zerkle et al., 2016; Moreras-Marti et al., 2022). In contrast, $\Delta^{33}S$ deviations associated with abiotic sulfide oxidation by O_2 are minor (0.037 ± 0.014 ‰: Eldridge and Farquhar, 2018). Therefore, minor sulfur isotopes may provide a powerful means to reconstruct sulfur cycling in hydrothermal systems.

The largest $\delta^{56}Fe$ variations in Earth's surface environments are caused by early diagenetic redox reactions (Johnson et al., 2020; Dauphas et al., 2024). More specifically, partial oxidation (abiotic or biotic) of Fe(II) generates a ^{56}Fe enriched Fe(III) pool, which then rapidly precipitates as Fe(III) (oxyhydr)oxide minerals with positive $\delta^{56}Fe$ signatures under circumneutral conditions (Johnson et al., 2020). Partial reduction of Fe(III) minerals generates Fe(II) with a negative $\delta^{56}Fe$ signature of down to −3 ‰ in equilibrium (Dauphas et al., 2017; Johnson et al., 2020). This can occur biologically during microbial dissimilatory Fe(III) reduction (Beard et al., 1999; Chanda et al., 2021; Crosby et al., 2005; Fortney et al., 2016). Moreover, the chemical reduction of Fe(III) (oxyhydr)oxides by sulfide, which is considered a critical process in sulfidic low-temperature and hydrothermal systems (Canfield and Berner, 1987; Poulton et al., 2004; Runge et al., 2023b, 2024), can produce $\delta^{56}Fe_{Fe(II)aq}$ of ca. -1 ‰ depending on mineralogy and reaction rates (McAnena et al., 2024).

If microbial Fe(III) reduction occurs in a closed system, the initial production of a light (i.e., ^{54}Fe enriched) Fe(II) pool can drive the residual iron pool towards heavier $\delta^{56}Fe$ compositions (Chever et al., 2015). Similarly, while the reductive dissolution of iron-bearing mineral particles initially yields isotopically light Fe(II), $\delta^{56}Fe$ compositions will progressively approach values closer to the iron source (Chever et al., 2015; McAnena et al., 2024). Moreover, the precipitation of isotopically light FeS can increase the $\delta^{56}Fe$ value of the residual iron pool (Butler et al., 2005; Severmann et al., 2006; Sivan et al., 2011; Roy et al., 2012). The $\delta^{56}Fe$ values of pyrite are additionally influenced by KIE and EIE. The KIE results in a more negative fractionation at faster precipitation rates, while the EIE causes a more positive fractionation at lower temperatures, which may be less expressed due to lower isotope exchange rates (Butler et al., 2005; Polyakov et al., 2007; Guilbaud et al., 2011; Syverson et al., 2013; Rolison et al., 2018; Mansor and Fantle, 2019). This inverse relationship between KIE and EIE during precipitation can diminish the apparent stable iron isotope fractionation, potentially blurring redox-dependent signals in hydrothermal pyrite.

The alteration of minerals by diagenetic hydrothermal fluids can affect sulfur and iron stable isotope records. For instance, in-situ sulfur isotope analysis of modern and ancient hydrothermal sulfides by secondary ion mass spectrometry (SIMS) indicates that high-temperature fluids can drive the recrystallization of framboidal pyrite and its associated evolution of $\delta^{34}S$ values towards heavier compositions (Liu et al., 2022; Nozaki et al., 2024). Moreover, the overgrowth of early diagenetic pyrite with secondary hydrothermal generations is common in these systems (Eldridge et al., 1988; Nozaki et al., 2020, 2024; Spinks et al., 2021; Meng et al., 2022; Martin et al., 2023). Notably, the few published stable iron isotope studies on sulfide minerals in ancient volcanogenic and sediment-hosted deposits did not reveal evidence for microbial iron cycling (Gagnevin et al., 2012; Otake et al., 2021), in contrast to studies on their modern counterparts (i.e., seafloor hydrothermal sulfide systems) (Toner et al., 2016). This might suggest that ancient deposits have experienced a more intense alteration of their initial iron isotope records. For instance, pyrite precipitation experiments at 300–450 °C demonstrated an increase in $\delta^{56}Fe$ value in pyrite over time due to EIE with $Fe(II)_{aq}$ during recrystallization (Syverson et al., 2013; Pokrovski et al., 2021). Such exchange reactions can significantly alter $\delta^{56}Fe$ signatures even at temperatures as low as 80 °C (Mansor and Fantle, 2019). These examples suggest a potential preservation bias against stable

isotope signatures of microbial sulfur and iron cycling. At the same time, they highlight that bulk analysis of isotopically zoned precipitates might yield mixed signals, potentially blurring microbial signatures (Marin-Carbonne et al., 2020; Nozaki et al., 2024). This underlines the need to assess the preservation potential of isotopic biosignatures in minerals from hydrothermal sulfide systems by combining textural and in-situ stable isotope analysis.

Here, we assessed the preservation of isotopic signatures indicative of microbial sulfur and iron cycling recorded in pyrite in the 390-million-year-old Rammelsberg deposit (Germany), a well-characterized example of sediment-hosted massive sulfides. We coupled textural analysis by reflected light (RL) and scanning electron microscopy (SEM) with in-situ SIMS triple sulfur ($\delta^{34}S$, $\Delta^{33}S$) and iron isotope data ($\delta^{56}Fe$). This combined approach revealed evidence for hydrothermal alteration of early diagenetic pyrite of likely microbial origin. We emphasize the challenges and potentials of coupled textural and in-situ sulfur and iron isotope analysis of pyrite for reconstructing microbial redox cycling in ancient hydrothermal sulfide systems, including some of the oldest rocks on Earth.

2. Geological context

The Rammelsberg sediment-hosted hydrothermal sulfide deposit is in the Harz Mountains, Northern Germany. The sulfide ore body occurs within a sedimentary succession deposited in the Goslar Trough – a continentally influenced semi-restricted marine basin that formed during regional extension before the Variscan orogeny (Ramdohr, 1953; Paul, 1975; Sperling, 1986; Walcher, 1986; Sáez et al., 2011; Moreno et al., 2019) (Fig. 1). The Rammelsberg deposit is hosted within the 'Wissenbacher Schiefer', a local subunit of the Middle Eifelian to Middle Givetian Goslar Formation (Buchholz and Luppold, 2008) (Fig. 1). The ore equivalent horizon (i.e., the unmineralized lateral extension of the ore body; Fig. 1) dominantly consists of shales (with minor carbonate and pyrite) interbedded with siltstones and fine-grained sandstones, interpreted as distal turbiditic sediments (Walcher, 1986; Large and Walcher, 1999; Sáez et al., 2011; Moreno et al., 2019). Redox-sensitive

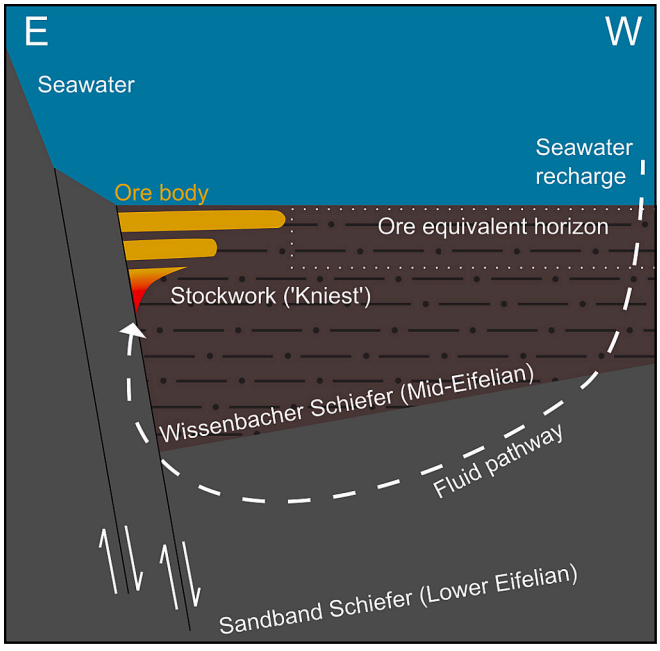

Fig. 1. Schematic of the Goslar Trough during the initial rift stage of the Variscan orogeny (not to scale). Hydrothermal fluid circulation and sulfide ore formation occurred during deposition of the Middle Eifelian Wissenbacher Schiefer. The sample analyzed in this study originates from the ore body. Redrawn after Sáez et al. (2011) and Moreno et al. (2019).

trace element characteristics (V, Mo, U) in the shales suggest oxic bottom waters with the redox boundary below the sediment surface (Sáez et al., 2011). Organic carbon (C_{org}) contents are relatively low (<1 wt %), which at least in parts may be due to C_{org} oxidation during TSR (Sáez et al., 2011).

The formation of the Rammelsberg sulfide ore body was tightly coupled to the subsidence of the Rhenohercynian basin (Large and Walcher, 1999; Moreno et al., 2019). Accordingly, metal-rich hydrothermal fluids were channeled to the seafloor via deeply rooted extensional faults. The 'Kniest' zone crosscuts the footwall shale horizon and likely served as the central feeder zone during ore formation (Large and Walcher, 1999; Moreno et al., 2019). The cyclic intercalation of the sulfide ores with partially replaced black shale layers and fragments demonstrates that the ore formation proceeded in several pulses and syngenetically to the deposition of the Wissenbacher Schiefer (Large and Walcher, 1999; Sáez et al., 2011).

The major minerals in the ore body are sphalerite [ZnS], galena [PbS], barite [$BaSO_4$], chalcopyrite [$CuFeS_2$], and pyrite [FeS_2], with pyrite as the dominant iron sulfide (Large and Walcher, 1999; Sáez et al., 2011; Moreno et al., 2019). Microthermometric analysis of fluid inclusions in the Kniest and sulfur isotope pairs between sphalerite, galena, and chalcopyrite in the ore body suggest minimum temperatures of 130–180 °C for the mineralizing brine (Nielsen, 1985; Muchez and Stassen, 2006). Sulfur input from hydrothermal sources is evident by the higher pyrite content of the Rammelsberg deposit (up to 25 wt.-%) compared to the ore equivalent horizon in the Wissenbacher Schiefer, which only has minor authigenic framboidal and euhedral pyrite (Walcher, 1986; Sáez et al., 2011). The fluid circulation was also associated with hydrothermal iron input, as evidenced by iron enrichment in chlorites from the Kniest compared to the ore equivalent horizon (Large and Walcher, 1999). Fe:S ratios in the ore equivalent horizon exceed the stoichiometry of pyrite, partly due to the presence of iron carbonates of possible hydrothermal origin (Large and Walcher, 1999; Sáez et al., 2011). Hydrothermal alteration of the ore equivalent horizon is also reflected in increased carbonate and silica content near the Kniest (Large and Walcher, 1999). Deformation of the Rammelsberg deposit occurred during the Variscan orogeny, although at a low metamorphic grade (up to 260 °C: Ramdohr, 1953; Muchez and Stassen, 2006).

3. Materials and methods

3.1. Reflected light (RL) and scanning electron microscopy (SEM)

The analyzed sample originates from the 'banded ore' of the Rammelsberg deposit (Goslar, Harz mountains, Germany), a UNESCO World Heritage site. It was stored in the rock collection of the Department of Geobiology at the University of Göttingen (sample ID: Rammelsberg 2120). Before reflected light (RL) and scanning electron microscopy (SEM), the sample was polished using 1 and 0.25 μm diamond paste. RL microscopy images were recorded using a Keyence VHX-6000 digital microscope at the University of Göttingen. SEM was performed using a Crossbeam 550 L SEM (Zeiss, Oberkochen, Germany) operating at an acceleration voltage of 20 kV and working distances of 9.1 mm. All micrographs were taken using the backscattered electron detector (BSD). The textural classification of the analyzed pyrite grains was based on SEM observation of the following criteria: 'framboid-like pyrite' includes sensu stricto framboids (i.e., spherical aggregates of microcrystals exhibiting a raspberry-like texture) and morphologically similar spherical grains; 'subhedral pyrite' has at least one well-developed crystal face (see Supplementary Fig. 1 for SEM images of all selected grains).

3.2. Secondary ion mass spectrometry (SIMS)

In total, 51 pyrite grains were analyzed for their iron isotope composition using the SIMS instrument (Cameca IMS 1280-HR) at the SwissSIMS facility of the University of Lausanne. 25 out of 51 pyrite

grains were additionally analyzed for their sulfur isotope composition using the same instrument. The sample was cut from a polished petrographic thin section using a diamond wire saw and embedded in indium in an aluminum sample mount. The topography of the sample mount's surface was assessed using a white light microscope and was less than 3 μm. Two reference standard grains (Balmat and Ruttan pyrite, Whitehouse and Fedo, 2007; Pasquier et al., 2024) were included in each sample mount, and the mounts were gold-coated before analysis. The placement of SIMS spots within the target grains was verified by SEM after the analysis (Supplementary Fig. 1). The uncertainties associated with the SIMS analyses presented in this study are shown as 2σ.

SIMS analyses of iron isotope compositions followed the procedure detailed in Decraene et al. (2021). Pyrite grains were sputtered by a ~3.0 nA primary O^- beam focused to a 2.5–3 μm spot. The isotopes of ^{52}Cr, ^{54}Fe, ^{56}Fe, and ^{57}Fe were measured in multicollection mode with three off-axis Faraday cups and one electron multiplier for ^{52}Cr. The mass resolving power (MRP) was set at ~6800 to resolve interferences on $^{54}Fe^+$ ($^{53}CrH^+$, MRP: +6088) and $^{56}Fe^+$ ($^{55}MnH^+$, MRP: +5118). The mass of $^{52}Cr^+$ was measured to correct the $^{54}Cr^+$ isobaric interference on $^{54}Fe^+$ (Marin-Carbonne et al., 2011), as some samples display relatively high Cr content. Iron isotope compositions are reported as per mil variations of $^{56}Fe/^{54}Fe$ ratios measured in the samples normalized to that of the international standard (Institute for Reference Materials and Measurements-014, IRMM-014; Eq. (1)).

$$\delta^{56}Fe = \left[\frac{\left(\frac{^{56}Fe}{^{54}Fe}\right)_{sample}}{\left(\frac{^{56}Fe}{^{54}Fe}\right)_{IRMM-014}} - 1 \right] * 1000 \quad (1)$$

One analysis consisted of 90 s of pre-sputtering, during which centering of the primary beam and calibration of the Faraday cups was performed, followed by 40 cycles of analyses (total of 300 s). Balmat ($\delta^{56}Fe_{true} = -0.40 \pm 0.01$ ‰: Whitehouse and Fedo, 2007) was used as a primary reference material to correct the instrumental mass fractionation (IMF) inherent to the SIMS technique. The IMF corrected (IMFcorr) for the unknowns (ukn; $\delta^{56}Fe_{ukn,IMFcorr}$) is calculated according to Eq. (2)

$$\delta^{56}Fe_{ukn,IMFcorr} = 1000 \bullet \left[\frac{1 + \frac{\delta^{56}Fe_{ukn,meas}}{1000}}{\alpha} - 1 \right] \quad (2)$$

where

$$\alpha = \frac{1}{n}\sum_{i=1}^{n} \frac{1 + \frac{\delta^{56}Fe_{RM,meas,i}}{1000}}{1 + \frac{\delta^{56}Fe_{RM,true}}{1000}} \quad (3)$$

and RM stands for reference material, *meas* for measured by SIMS, *n* is the total number of measurements performed on the reference material throughout the SIMS session, and *true* refers to the bulk ratio of the reference material determined by Multi Collector Inductively Coupled Mass Spectrometry (MC-ICP-MS). The reproducibility of the primary standard was ±0.19 ‰ (July 2022 session).

SIMS analysis of sulfur isotope compositions followed an established routine procedure (Whitehouse, 2013). A Cs^+ primary beam of ~1.1 nA intensity was focused to a spot of approximately 10–15 μm. The typical $^{32}S^-$ intensity was between 8.2×10^8 and 1.3×10^9 counts per second for sulfide. The $^{32}S^-$, $^{33}S^-$, and $^{34}S^-$ were measured in multicollection mode with three off-axis Faraday cups. The mass resolution was set to ~5000 to resolve the isobaric interferences due to the hydride contribution on $^{33}S^-$ ($^{32}SH^-$, MRP: +3911). A typical analysis consisted of two minutes of pre-sputtering in raster mode and data acquisition in 40 cycles of five seconds each. The background of the detectors was measured during the pre-sputtering and was then corrected for each analysis. Sulfur isotope compositions are reported as per mil variations of $^{34}S/^{32}S$ and $^{33}S/^{32}S$ ratios measured in the samples normalized to that of the international standard (Vienna-Canyon Diablo Troilite, V-CDT; Eq. (4))

$$\delta^{3x}S = \left[\frac{\left(\frac{^{3x}S}{^{32}S}\right)_{sample}}{\left(\frac{^{3x}S}{^{32}S}\right)_{V-CDT}} - 1 \right] * 1000 \quad (4)$$

where x = 33 or 34.

The internal precision achieved under these conditions was better than ±0.16 ‰ for $\delta^{34}S$ and better than ±0.12 ‰ for $\delta^{33}S$ values. Several pyrite reference materials (Maine: $\delta^{34}S = -20.61 \pm 0.05$ ‰, $\delta^{33}S = -10.63 \pm 0.02$ ‰; Spain: $\delta^{34}S = -1.56 \pm 0.26$ ‰, $\delta^{33}S = -0.78 \pm 0.13$ ‰; and Balmat: $\delta^{34}S = +15.84 \pm 0.92$ ‰, $\delta^{33}S = +8.12 \pm 0.48$ ‰; Muller et al., 2017) were measured to determine the reference mass discrimination line, from which $\Delta^{33}S$ values were calculated. Balmat was used as a primary reference material to correct for IMF, and $\delta^{33}S_{IMFcorr}$ and $\delta^{34}S_{IMFcorr}$ were both calculated following the procedure described above for $\delta^{56}Fe_{ukn,IMFcorr}$. Ruttan was used as a secondary reference material to crosscheck the instrumental stability and calibration. The reproducibility was found to be ±0.17 ‰ ($\delta^{34}S$) and ± 0.28 ‰ ($\delta^{33}S$) for the primary standard and ± 0.28 ‰ ($\delta^{34}S$) and ± 0.26 ‰ ($\delta^{33}S$) for the secondary standard (September 2022 session). The $\Delta^{33}S$ values presented in this article were calculated according to Eq. (5). The uncertainties associated with the $\Delta^{33}S$ values are shown as the square root of the sum of the squared internal and external errors for each sulfur isotope.

$$\Delta^{33}S = \delta^{33}S - 1000 * \left[\left(1 + \left(\frac{\delta^{34}S}{1000} \right)^{0.516} \right) - 1 \right] + 0.013 \quad (5)$$

4. Results

4.1. Reflected light (RL) microscopy and scanning electron microscopy (SEM)

RL microscopy revealed the presence of layers rich in pyrite, chalcopyrite, sphalerite, and galena (Fig. 2A). Pyrite occurred as framboid-like and subhedral grains (Fig. 2B-D). Locally, the sample contained pyrite-bearing black shale fragments (Fig. 2D). Framboid-like pyrite was generally ca. 10 to 20 μm in size (Fig. 3A; Supplementary Fig. 1). Notably, some framboid-like pyrite did not show the characteristic raspberry-like internal texture observed in pristine framboids (Fig. 3A; Supplementary Fig. 1). Subhedral pyrite was 10 to several tens of μm in diameter (Figs. 3C-D, Supplementary Fig. 1). Subhedral pyrite locally overgrows framboid-like pyrite (Fig. 3B) and displays growth zonation (Fig. 3D). Notably, the distribution of pyrite morphotypes across the sample is heterogeneous (Fig. 4). While framboid-like pyrite is evenly distributed, subhedral pyrite seems to be particularly abundant in chalcopyrite-rich layers.

4.2. Secondary ion mass spectrometry (SIMS)

Microscale $\delta^{34}S$ values in pyrite ranged from −15.13 ‰ to +18.77 ‰ (median = +15.03 ‰; average ± 1SD = +12.62 ± 7.24 ‰; n = 25; Table 1, Fig. 5). Framboid-like pyrite varied between −15.13 ‰ and + 17.01 ‰ (median = +14.99 ‰; average ± 1SD = +12.16 ± 8.28 ‰; n = 14). Subhedral pyrite ranged from −0.30 to +18.77 ‰ (median = +15.98 ‰; average ± 1SD = +13.21 ± 6.01 ‰; n = 11) (Table 1; Fig. 5). The analyzed pyrite grains showed large variations in microscale $\delta^{56}Fe$ values ranging from −1.30 to +2.19 ‰ (median = +0.77 ‰; average ± 1SD = +0.55 ± 0.81 ‰; n = 51; Table 1; Fig. 5). The $\delta^{56}Fe$ value of framboid-like pyrite varied between −1.15 ‰ and + 1.99 ‰ (median = +0.39 ‰; average ± 1SD = +0.43 ± 0.78 ‰; n = 32). Subhedral pyrite ranged from −1.30 to +2.19 ‰ (median = +0.99 ‰; average ± 1SD =

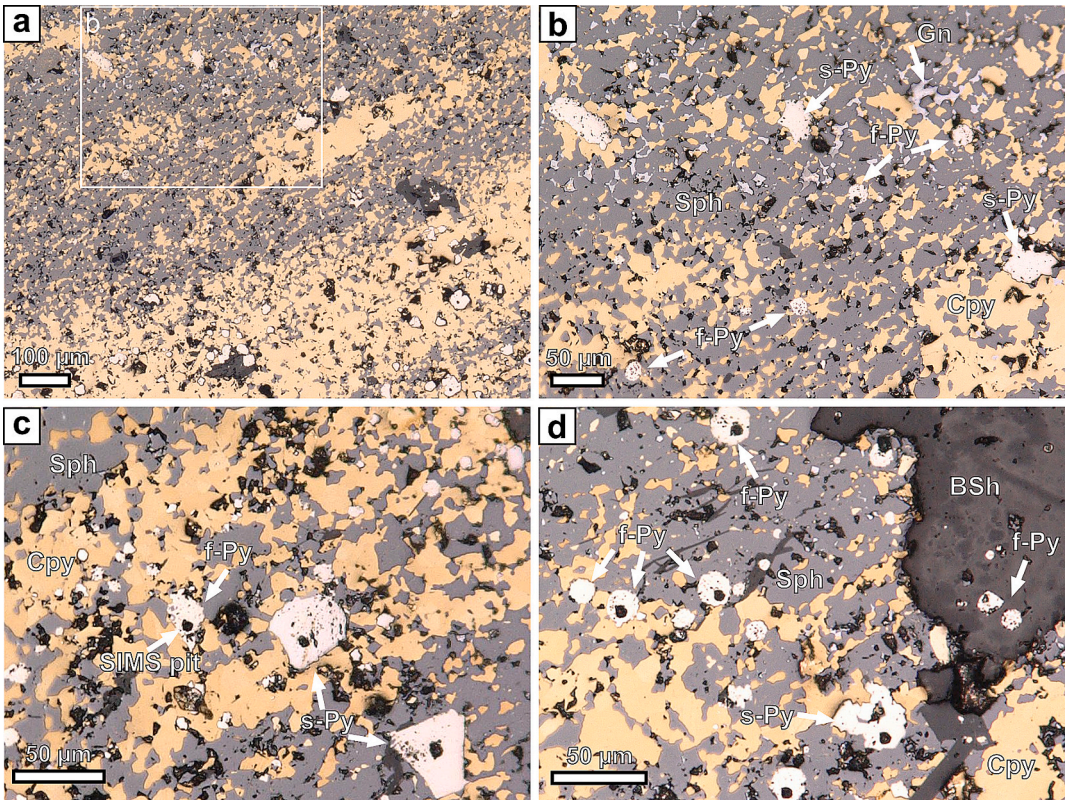

Fig. 2. Reflected light (RL) microscopy images of sulfides in the Rammelsberg deposit. A: Layered sulfide ore consisting of alternating (chalco)pyrite (brass-colored) and sphalerite with accessory galena (greyish colors); B-D: Close-up views of chalcopyrite, sphalerite (Sph), galena (Gn), framboid-like and subhedral pyrite (f-Py and s-Py, respectively). Note the pyrite-bearing black shale (BSh) fragment, likely a remnant of the precursor sediment. The dark pits in the pyrite grains (one example highlighted in C) are the secondary ion mass spectrometry (SIMS) analysis spots (~3–4 µm each).

0.84 ± 0.76 ‰; $n = 19$) (Table 1; Fig. 5). All SIMS data are available in the Supplementary Materials.

5. Discussion

5.1. Spatial relations and growth sequence of pyrite

The co-occurrence of multiple pyrite morphotypes in hydrothermal systems is commonly interpreted as a growth sequence (e.g., early diagenetic framboids vs. late diagenetic/hydrothermal euhedral grains: Eldridge et al., 1988, 1993; Sawlowicz, 1993; Nozaki et al., 2024). Indeed, the Rammelsberg deposit formed in a sediment-hosted hydrothermal sulfide system characterized by the deposition of silt- and clay-rich sediments affected by repeated pulses of sulfidic hydrothermal fluid circulation (Ramdohr, 1953; Large and Walcher, 1999; Sáez et al., 2011) (Fig. 1). Therefore, pyrite in the Rammelsberg deposit could have formed in multiple steps, driven by (microbial) low-temperature processes and hot, metal-rich fluids.

Early diagenetic pyrite formation in the Rammelsberg system is evident from the presence of framboidal and euhedral grains in the ore equivalent horizon of the Wissenbacher Schiefer (Large and Walcher, 1999). In our sample, this pyrite generation may be reflected by the grains within the black shale fragment (Fig. 2D, 4). Overgrowths of subhedral on framboid-like pyrite demonstrate that the latter formed earlier (Fig. 3B). Moreover, growth zonation in subhedral pyrite (Fig. 3D) suggests that the relative influence of different pyrite formation mechanisms and/or fluid conditions might even vary during the growth of individual grains, as implied by commonly observed zonation features in pyrite elsewhere (e.g., England et al., 2002; Marin-Carbonne et al., 2014; Reinhardt et al., 2024). This is supported by the predominant spatial association of subhedral pyrite with chalcopyrite (Fig. 4), suggesting paragenetic precipitation in different events or under different microenvironmental conditions than framboid-like pyrite. Due to the absence of the characteristic raspberry-like internal texture in some framboid-like pyrite (Figs. 2C-D, 3A-B), it cannot be excluded that some of these grains are analogous to similarly sized spheroidal pyrite from pyritization experiments in cultures of sulfur- and iron-cycling microorganisms, in the presence of organic matter, or in black smokers (Berg et al., 2020; Runge et al., 2024; Truong et al., 2024). However, considering the presence of multiple pyrite generations, it seems plausible that most of these framboid-like grains were recrystallized or cemented by a secondary generation of pyrite due to interaction with sulfidic fluids, as previously suggested (Ramdohr, 1953; Runge et al., 2023a). These observations demonstrate a complex pyrite formation sequence from early framboid-like to later subhedral pyrite.

5.2. Hydrothermal versus microbial sulfide sources: Insights from triple sulfur isotopes ($\delta^{34}S$, $\Delta^{33}S$)

Due to the complex pyrite formation sequence in the Rammelsberg deposit, bulk (bio)geochemical approaches may not allow for resolving potential isotopic variabilities but yield average compositions, even in the case of isolated grains. Microscale in-situ approaches, such as those presented here, could be much better suited to disentangle potential isotopic fingerprints of microbial redox cycling in pyrite from hydrothermally influenced environments (e.g., Eldridge et al., 1988, 1993; Marin-Carbonne et al., 2020; Nozaki et al., 2020, 2024).

The range of $\delta^{34}S$ values in pyrite measured in this study ($\delta^{34}S \approx -15$ to +19 ‰; Table 1) matches previously analyzed bulk and in-situ pyrite $\delta^{34}S$ values from the Rammelsberg deposit (−20 ‰ to +20 ‰: Anger et al., 1966; Nielsen, 1985; Eldridge et al., 1988; Large and Walcher, 1999) and comparable to other Phanerozoic sediment-hosted

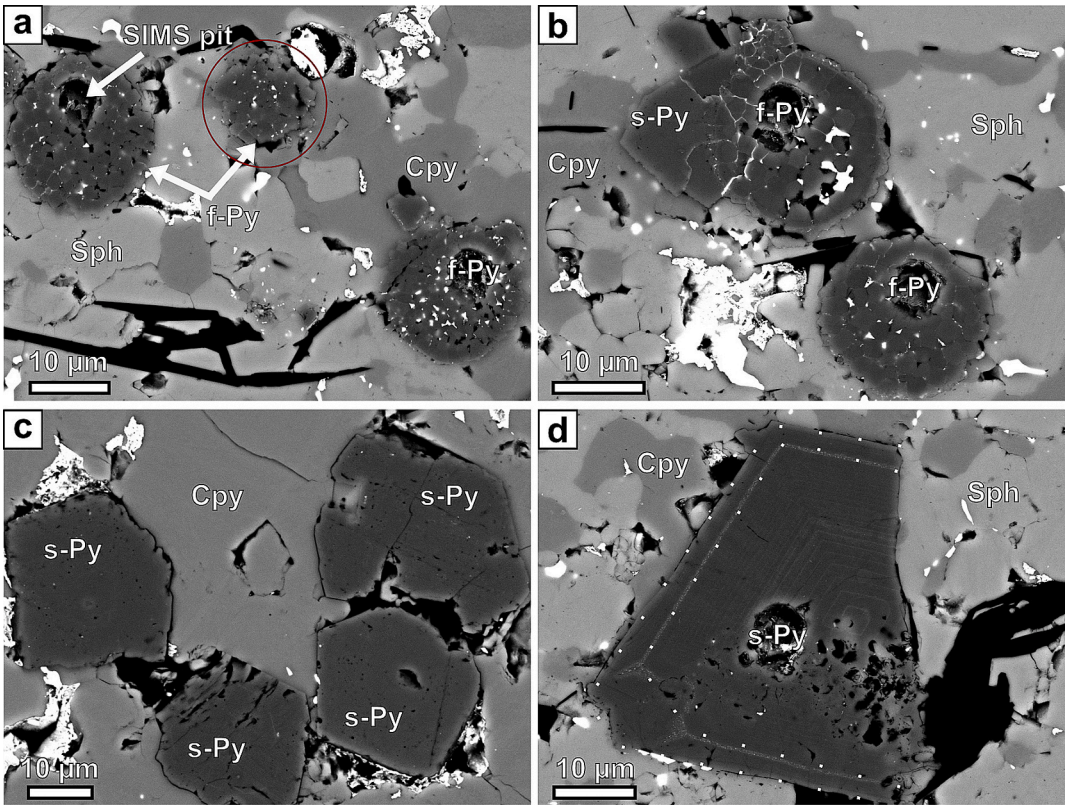

Fig. 3. Scanning electron microscopy (SEM) photographs of pyrite textures in the Rammelsberg deposit. A: framboid-like pyrite (f-Py) in sphalerite (Sph) and chalcopyrite (Cpy) dominated matrix; B: framboid-like pyrite with subhedral pyrite (s-Py) overgrowth, indicating an earlier formation of f-Py; C: s-Py in Cpy matrix; D: s-Py with growth zonation texture and a recrystallized rim (white dotted line). Note that some f-Py appears recrystallized or cemented by a secondary generation (example highlighted in A, red circle). The dark pits in the pyrite grains (example highlighted in A) are the secondary ion mass spectrometry (SIMS) analysis spots (~3–4 µm each). The bright materials around grain boundaries and cracks are remnants of gold coating for SIMS analysis. (For interpretation of the references to colour in this figure legend, the reader is referred to the web version of this article.)

hydrothermal sulfides (e.g., Buschendorf et al., 1963; Goodfellow, 1987; Kelley et al., 2004). In the Rammelsberg deposit, this range was interpreted to reflect a co-occurrence of sulfide from MSC ($\delta^{34}S_{pyrite} < 0$ ‰) and TSR ($\delta^{34}S_{pyrite} \approx +5$ to $+20$ ‰) of seawater ($\delta^{34}S_{sulfate} = +20.4 \pm 0.30$ ‰; Wu et al., 2014) or sedimentary sulfate in the deep subsurface (Eldridge et al., 1988; Sáez et al., 2011). The co-occurrence of sulfide from MSC and TSR in pyrite from the Rammelsberg deposit is plausible since periods of low-temperature marine sedimentation (conducive to MSC) likely alternated with periods of hydrothermal fluid circulation (conducive to TSR) (Large and Walcher, 1999). Thus, the range of $\delta^{34}S$ values observed here could be explained by the (near) complete reduction of seawater sulfate or the partial reduction of a ^{34}S-enriched sulfate reservoir by DSR or TSR. Such enrichment could have resulted from Rayleigh distillation in the porewater under closed system conditions (Sansjofre et al., 2016; Thomazo et al., 2019). Closed system conditions could have been favored in the Rammelsberg system via sediment burial and the semi-restricted paleogeographic situation of the Goslar Trough, limiting exchange with the seawater sulfate pool (Walcher, 1986; Sáez et al., 2011; Moreno et al., 2019).

To investigate the role of TSR and DSR in the Rammelsberg system, we modeled the evolution of sulfide $\delta^{34}S$ versus $\Delta^{33}S$ during Rayleigh-type isotope distillation (Fig. 7). We assumed an initial $\delta^{34}S_{sulfate}$ value of $+20.4 \pm 0.30$ ‰ and $\Delta^{33}S = +0.026 \pm 0.094$ ‰ for the contemporaneous middle Eifelian seawater as derived from carbonate-associated sulfate (Wu et al., 2014). Equilibrium fractionation factors were applied for low temperature DSR (20 °C) and TSR in the range of minimum fluid temperature estimates in the Rammelsberg ore-forming system (130 °C and 180 °C) ($^{34}\alpha[H_2S\text{-}SO_4^{2-}] = 0.9287$, 0.9600, 0.9676, and $^{33}\lambda = 0.5147$, 0.5151, 0.5153, respectively; Johnston et al., 2007; Eldridge et al., 2021). Considering the maximum recorded fractionation ($\Delta^{34}S_{sulfate\text{-}pyrite} \approx 35$ ‰) and the uncertainties of the $\Delta^{33}S$ values, our triple sulfur isotope data are consistent with either DSR or TSR, or sulfide contributions from both (Fig. 7).

A strong contribution from TSR is supported by the much higher pyrite content (up to 25 wt.-%) in the Rammelsberg deposit compared to the ore equivalent horizon, and the ore body's organic carbon depletion alongside secondary carbonates, likely due to carbon oxidation during TSR (Walcher, 1986; Machel et al., 1995; Sáez et al., 2011; Cai et al., 2022). Moreover, chalcopyrite in the Rammelsberg deposit, most likely a hydrothermal precipitate (e.g., Large and Walcher, 1999), is consistently heavy (i.e., $\delta^{34}S \approx 13$ ‰; Eldridge et al., 1988), supporting a TSR origin of the paragenetic subhedral pyrite ($\delta^{34}S = -0.30$ to $+18.77$ ‰) (Fig. 4). TSR also generally produces nodular or euhedral pyrite grains, possibly exhibiting growth zonation (Liang et al., 2024), as observed here (Fig. 3D). However, the multiple generations and morphological variety of pyrite suggest TSR was not the only driver of pyrite formation (Figs. 2–3). The most negative $\delta^{34}S$ value (−15.13 ‰) presented in this study appears in framboid-like pyrite (Fig. 5, Table 1), which is demonstrably an early phase (Fig. 3B). Since pyrite framboids most commonly form during early diagenetic MSC (Popa et al., 2004; Maclean et al., 2008; Wacey et al., 2015; Duda et al., 2016; Rickard, 2019; Marin-Carbonne et al., 2022), it seems plausible that this grain inherited its $\delta^{34}S$ value from microbial processes in the precursor sediments of the Rammelsberg deposit. Indeed, MSC is recorded in highly fractionated $\delta^{34}S_{pyrite}$ values of −32.7 to +53.7 ‰ in the hydrothermally unaffected Wissenbacher Schiefer (Anger et al., 1966). Considering the evidence for framboid recrystallization and overgrowth by subhedral pyrite (Fig. 3A-B), we interpret the isotopically lightest pyrite in our study ($\delta^{34}S =$

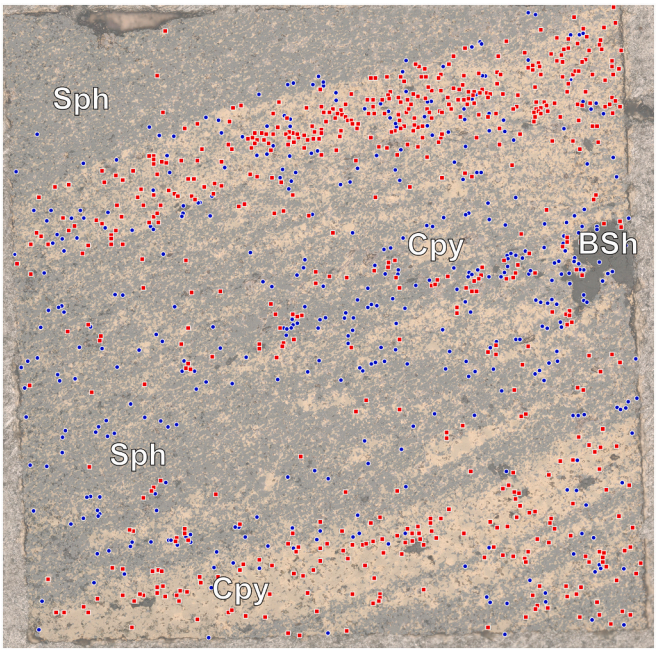

Fig. 4. Reflected light microscopy mosaic image and pyrite morphotype distribution. Framboid-like pyrite (blue circles) was evenly distributed. Subhedral pyrite (red squares) was more abundant in chalcopyrite-rich zones (Cpy, brass-colored areas) than in sphalerite-rich zones (Sph, grey). This implies a paragenetic relationship between subhedral pyrite and chalcopyrite. The black shale fragment (BSh) likely represents a remnant of the precursor sediment. The field of view is ~2.5 mm. (For interpretation of the references to colour in this figure legend, the reader is referred to the web version of this article.)

Table 1
Iron and sulfur isotope compositions of framboid-like and subhedral pyrite (f-Py and s-Py, respectively) in the Rammelsberg deposit. All data points are available in the Supplementary Materials (n = number of analyses).

	Framboid-like (f-Py)	Subhedral (s-Py)	All
δ^{56}Fe Min [‰]	−1.15	−1.30	−1.30
δ^{56}Fe Max [‰]	1.99	2.19	2.19
δ^{56}Fe Average [‰]	0.43	0.76	0.55
δ^{56}Fe Median [‰]	0.39	0.99	0.77
δ^{56}Fe 1σ [‰]	0.78	0.84	0.81
δ^{56}Fe n	32	19	51
δ^{34}S Min [‰]	−15.13	−0.30	−15.13
δ^{34}S Max [‰]	17.01	18.77	18.77
δ^{34}S Average [‰]	12.16	13.21	12.62
δ^{34}S Median [‰]	14.99	15.98	15.03
δ^{34}S 1σ [‰]	8.28	6.01	7.24
δ^{34}S n	14	11	25
Δ^{33}S Min [‰]	−0.03	−0.21	−0.21
Δ^{33}S Max [‰]	0.21	0.26	0.26
Δ^{33}S Average [‰]	0.10	0.01	0.06
Δ^{33}S Median [‰]	0.09	0.00	0.08
Δ^{33}S 1σ [‰]	0.07	0.16	0.12
Δ^{33}S n	14	11	25

−15.13 ‰, framboid-like) as an originally early diagenetic framboid that interacted with ^{34}S-enriched hydrothermal sulfide.

In this scenario, the similar median δ^{34}S compositions of framboid-like and subhedral pyrite (Table 1, Fig. 3A) could reflect an early diagenetic microbial pyrite generation with initial δ^{34}S compositions of <0 ‰ that experienced isotope exchange with ^{34}S-enriched hydrothermal fluids (δ^{34}S > 0 ‰) during recrystallization, and/or signal mixing due to cementation and overgrowth by a secondary subhedral generation (Eldridge et al., 1988; Nozaki et al., 2020, 2024; Liu et al., 2022; Meng et al., 2022; Martin et al., 2023). Such an evolution is consistent with previous interpretations from the Rammelsberg deposit and other sediment-hosted hydrothermal sulfide deposits, as well as TSR-affected sedimentary basins (Anger et al., 1966; Nielsen, 1985; Eldridge et al., 1988; Large and Walcher, 1999; Lyons et al., 2006; Sáez et al., 2011; Paiste et al., 2024). If correct, the strong similarity of most framboid-like pyrite with subhedral pyrite suggests a pervasive alteration of original framboids. This may have resulted in the unimodal δ^{34}S distribution around near-seawater δ^{34}S values, independent of pyrite morphology in our study (Fig. 6). Thus, the most likely scenario is a two-step process involving early diagenetic MSC-driven pyrite formation during low-temperature conditions, followed by TSR-driven framboid recrystallization and subhedral pyrite formation.

5.3. *Hydrothermal versus early diagenetic pyrite formation - insights from iron isotopes (δ^{56}Fe)*

The two-step model of MSC during early diagenesis, followed by TSR, allows for different predictions concerning the iron cycle during pyrite formation in the Rammelsberg system: either sulfidic hydrothermal fluids drove the pyritization of sedimentary iron-bearing precursors, or hydrothermal Fe(II) delivery was involved in secondary pyrite formation with TSR-derived sulfide, or both.

Microscale δ^{56}Fe values in sedimentary pyrite typically range between ca. -4 ‰ to +4 ‰ (Dupeyron et al., 2023). Sedimentary pyrite forms via the reaction of aqueous FeS (FeS_{aq}) with polysulfides or H_2S (Rickard, 1975, 1997; Luther, 1991) or surface-mediated sulfidation of Fe(III) (oxyhydr)oxides (Peiffer et al., 2015; Wan et al., 2017). The FeS_{aq} precursor commonly results from mackinawite (FeS_m) dissolution (Rickard, 1997). FeS_m, in turn, can either precipitate from negative δ^{56}Fe pore water $Fe(II)_{aq}$ or positive δ^{56}Fe Fe(II) after the complete reduction of Fe(III) (oxyhydr)oxides (Crosby et al., 2007; Guilbaud et al., 2011; Marin-Carbonne et al., 2020). Hence, the δ^{56}Fe variation in sedimentary pyrite might reflect the early diagenetic or hydrothermal pyritization of isotopically different precursors (Marin-Carbonne et al., 2020; Decraene et al., 2021) (Fig. 6). Iron redox reactions during the production of pyrite precursors affect its δ^{56}Fe records via the low-temperature Fe(II)-Fe(III) equilibrium ($\Delta^{56}Fe_{Fe(III)\text{-}Fe(II)} = +3$ ‰; Dauphas et al., 2017; Johnson et al., 2020). Moreover, rapid pyrite precipitation can induce a KIE of down to $\Delta^{56}Fe_{pyrite\text{-}Fe(II)aq} = -3$ ‰ (Guilbaud et al., 2011). Isotope exchange with porewater Fe(II) induces an opposing EIE of $\Delta^{56}Fe_{pyrite\text{-}Fe(II)aq} = +6.1$ ‰ at 25 °C (Polyakov and Soultanov, 2011), although this is not expressed in natural environments due to slow exchange rates at low temperatures. Accordingly, the strongest fractionations in sedimentary pyrite are commonly interpreted to reflect precursors cycled through multiple redox cycles and/or the combined effects of Fe(III) reduction and rapid pyrite precipitation (Johnson et al., 2008; Mansor and Fantle, 2019; Dupeyron et al., 2023).

If the δ^{56}Fe variation in our sample results from isotopically different precursors, the measured pyrite endmembers would approximate the composition of the heavier and lighter precursors. Isotopically heavy precursors may derive from the complete dissolution of Fe(III) (oxyhydr) oxides like magnetite (Poulton et al., 2004; Runge et al., 2023b, 2024), which is an accessory mineral in the Rammelsberg deposit (Ramdohr, 1953). Isotopically lighter precursors could derive from partial Fe(III) reduction by dissimilatory Fe(III) reduction or reducing hydrothermal fluids (Beard et al., 1999; Butler et al., 2005; McAnena et al., 2024), with or without an additional KIE from pyrite precipitation. The difference between these endmembers in our sample is +3.49 ‰, similar to the Fe (III)-Fe(II) equilibrium. Therefore, the pyritization of isotopically distinct precursors can explain the overall δ^{56}Fe variability in our study. Notably, the similar δ^{56}Fe ranges of framboid-like and subhedral pyrite (Figs. 5, 6) suggest this could apply to all observed pyrite morphotypes. The production of such precursors requires iron redox cycling in the sediment, which is dominantly driven by microorganisms during early diagenesis (Picard et al., 2016; Berg et al., 2020; Planavsky et al., 2021; Kappler et al., 2021), consistent with periods of low-temperature

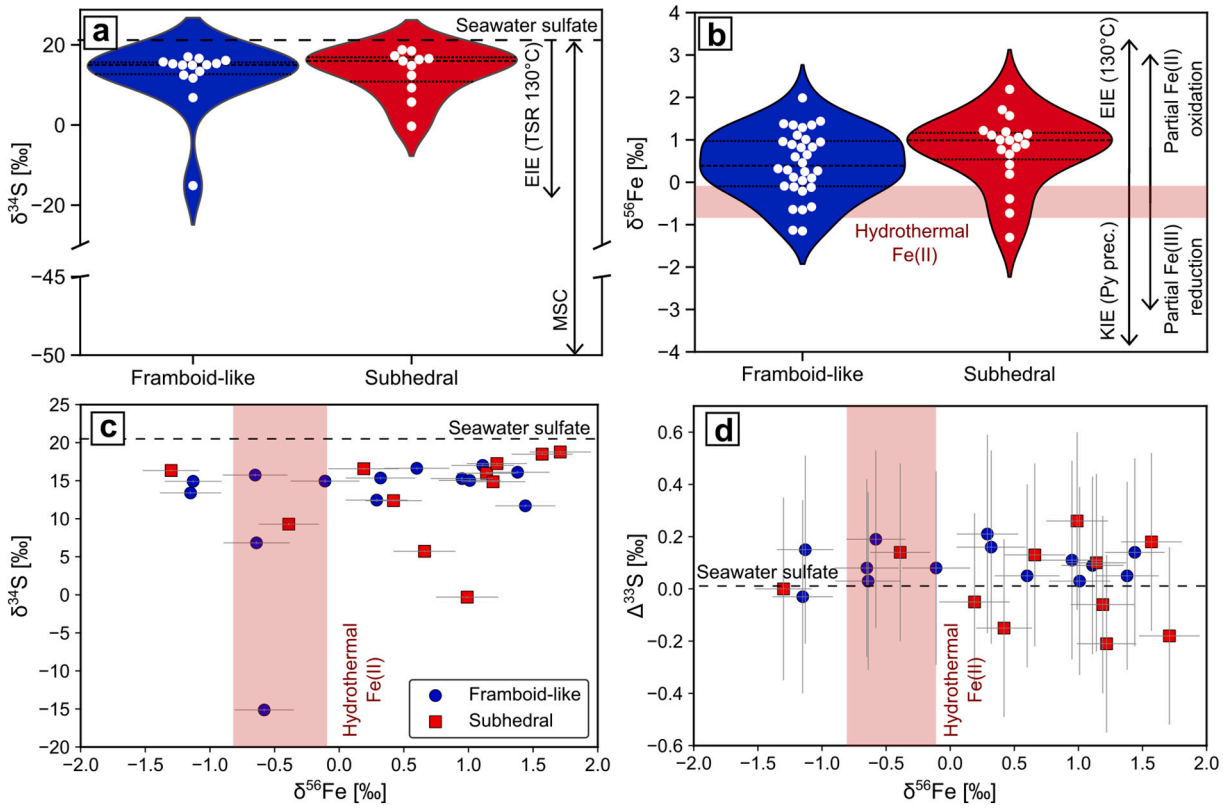

Fig. 5. Pyrite sulfur ($\delta^{34}S$, $\Delta^{33}S$) and iron ($\delta^{56}Fe$) isotope composition for framboid-like (blue circles) and subhedral (red squares) pyrite in the Rammelsberg deposit. A, B: Violin plots of sulfur isotope composition and systematics. Starting from middle-Eifelian seawater ($\delta^{34}S = +20.4‰$; Wu et al., 2014), equilibrium isotope effects (EIE) during thermochemical sulfate reduction (TSR) can generate pyrite with down to $\delta^{34}S \approx -19$ ‰ at 130 °C (Eldridge et al., 2016), the minimum fluid temperature reconstruction for the Rammelsberg system (Muchez and Stassen, 2006). Microbial sulfur cycling (MSC) could generate pyrite down to $\delta^{34}S \approx -50$ ‰. B: Violin plots of iron isotope composition and systematics. Kinetic isotope effects (KIE) during pyrite precipitation can generate pyrite with $\delta^{56}Fe < -3.0$ ‰ relative to the hydrothermal Fe(II) source (−0.8 to −0.1 ‰) (Guilbaud et al., 2011). Full expression of the EIE between pyrite and hydrothermal Fe(II) during pyrite precipitation and mineral-fluid interactions may generate pyrite with up to $\delta^{56}Fe = +3.3$ ‰ at 130 °C (Polyakov and Soultanov, 2011). Iron redox reactions affecting pyrite precursors can generate pyrite with $\delta^{56}Fe = -3$ to +3 ‰ (Johnson et al., 2020). C: $\delta^{56}Fe$ vs. $\delta^{34}S$ cross plot. D: $\delta^{56}Fe$ vs. $\Delta^{33}S$ cross plot. The violin plot's middle lines represent the median values. (For interpretation of the references to colour in this figure legend, the reader is referred to the web version of this article.)

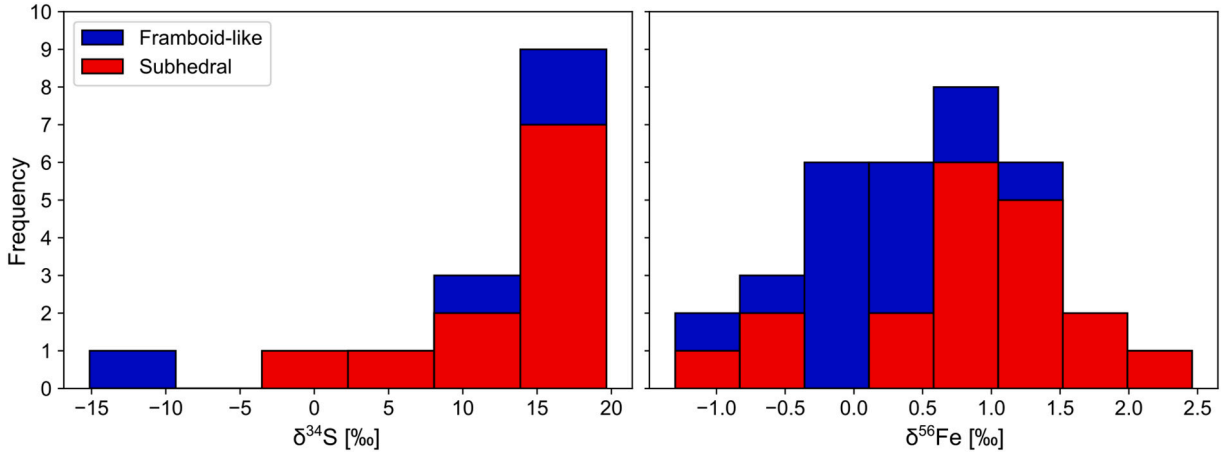

Fig. 6. Histograms of sulfur ($\delta^{34}S$) and iron ($\delta^{56}Fe$) isotope compositions of the different pyrite morphotypes from the Rammelsberg deposit. Each histogram's number of bins (k) was selected following the Rice rule ($k = 2 \times n^{1/3}$; n = number of analyses).

conditions in the Rammelsberg system. Thus, the $\delta^{56}Fe$ variability displayed here may record a diagenetic fractionation of the sedimentary iron pool by microbial activity.

Alternatively, pyrite could have precipitated from hydrothermal Fe (II). The $\delta^{56}Fe$ of such pyrite should variably express KIE and EIE as a function of precipitation rate (Syverson et al., 2013; Mansor and Fantle, 2019; Pokrovski et al., 2021). Pyrite in recent seafloor hydrothermal sulfides typically has $\delta^{56}Fe$ values between ca. -2.0 and 0.0 ‰ (Rouxel et al., 2004, 2008; Dauphas et al., 2017). Within the temperature estimates for the Rammelsberg system of 130 to 180 °C (Muchez and Stassen, 2006), the apparent isotope fractionation during pyrite precipitation should be $\Delta^{56}Fe_{pyrite\text{-}Fe(II)aq} \approx -1.9$ to −1.5 ‰ (Syverson et al.,

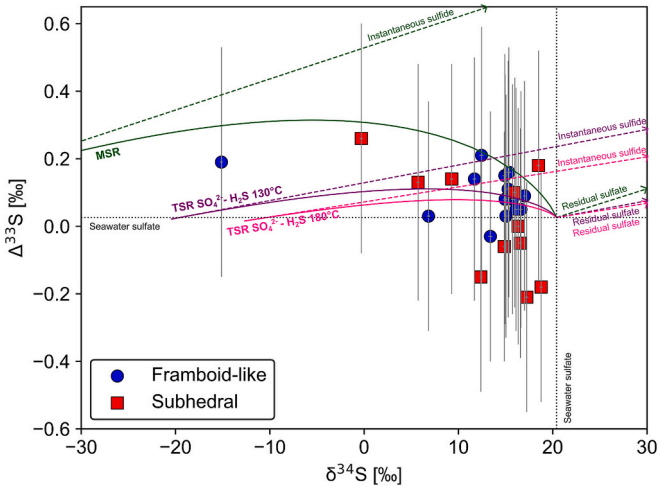

Fig. 7. Triple sulfur isotope plot and model results for closed-system Rayleigh distillation during thermochemical sulfate reduction (TSR) and dissimilatory sulfate reduction (DSR). The modeled fractionation trends are achieved using an initial $\delta^{34}S_{sulfate} = +20.4$ ‰, $\Delta^{33}S = +0.026$ ‰ for middle Eifelian seawater (Wu et al., 2014). We assumed equilibrium conditions for DSR at 20 °C and TSR at 130 °C and 180 °C ($^{34}\alpha[H_2S\text{-}SO_4^{2-}] = 0.9287$, 0.9600, 0.9676, and $^{33}\lambda = 0.5147$, 0.5151, 0.5153, respectively). Dashed lines refer to the evolution of sulfur species during closed-system DSR and TSR. Instantaneous sulfide corresponds to sulfide formed at the respective time point. Residual sulfate refers to the corresponding sulfate reservoir at that time point. The bold lines are the cumulated pyrite predicted by the model.

2013; Mansor and Fantle, 2019), resulting in $\delta^{56}Fe_{pyrite} \approx -2.7$ to -1.6 ‰ at typical $\delta^{56}Fe$ values of $Fe(II)_{aq}$ in recent hydrothermal fluids ($\delta^{56}Fe_{Fe(II)aq} = -0.8$ to -0.1 ‰.: Severmann et al., 2004; Johnson et al., 2008; Rouxel et al., 2008) (Fig. 5B). This is inconsistent with the $\delta^{56}Fe$ variability and the strongly positive values we observed (Table 1; Figs. 5, 6). Hence, the KIE associated with rapid pyrite precipitation from hydrothermal Fe(II) is not expressed in $\delta^{56}Fe$ data. On the other hand, the expected $\Delta^{56}Fe_{pyrite\text{-}Fe(II)aq}$ equilibrium fractionation in the Rammelsberg system ranges from +2.7 to +3.4 ‰ at 180 and 130 °C, respectively (Polyakov and Soultanov, 2011) (Fig. 5B). Therefore, if pyrite precipitated from hydrothermal fluids, it reflects various degrees of equilibration with Fe(II), which drives pyrite $\delta^{56}Fe$ to more positive values with lower fractionation factors but increased isotope exchange rates at higher temperatures. Moreover, it cannot be excluded that precipitation of isotopically light pyrite elsewhere in the system enriched the residual hydrothermal Fe(II) in ^{56}Fe (Butler et al., 2005; Severmann et al., 2006; Sivan et al., 2011; Roy et al., 2012), resulting in relatively heavy pyrite.

Partial equilibration with hydrothermal Fe(II) is supported by the lower median $\delta^{56}Fe$ in framboid-like pyrite compared to subhedral pyrite (+0.39 vs. +0.99 ‰; Table 1) suggesting the latter may be more affected by EIE, and the common mode of both morphotypes at ca. +1 ‰ (Fig. 5). This is consistent with textural evidence for framboid-like pyrite recrystallization and overgrowth by subhedral pyrite (Fig. 3). Thus, the $\delta^{56}Fe$ variability between morphotypes may be due to a stronger expression of isotope exchange and/or lower relative precipitation rates in later pyrite generations. Pyrite formation rates depend on various parameters, including temperature, pH, E_h, pyrite saturation, iron/sulfide ratio, type and stoichiometry of the iron source, trace metal abundance, as well as content and composition of organic matter (Berner, 1984; Canfield et al., 1992; Benning et al., 2000; Wan et al., 2017; Baya et al., 2021; Nie et al., 2023; Wang et al., 2023; Domingos et al., 2023; Runge et al., 2023b, 2024). Notably, pyritization rates also affect pyrite morphology (Murowchick and Barnes, 1987; Wang and Morse, 1996; Wang et al., 2022; Domingos et al., 2023; Runge et al., 2023b, 2024). Thus, variations in pyritization rates among different microenvironments within a sedimentary body and over time during progressive diagenesis can lead to the co-occurrence of various pyrite morphotypes after compaction (Chang et al., 2022). Framboidal pyrite in sediments and sedimentary rocks is usually considered an early diagenetic microbially induced precipitate characterized by rapid nucleation (e.g., Rickard, 2019). On the other hand, subhedral to euhedral pyrite grains, such as those presented here (Figs. 2, 3), commonly result from the slow growth of microcrystalline grains or framboid recrystallization (Sawlowicz, 1993; Domingos et al., 2023). Accordingly, framboid-like pyrite should reflect a dominant expression of KIE (i.e., lower $\delta^{56}Fe$), while subhedral pyrite expresses a stronger EIE (i.e., higher $\delta^{56}Fe$) (Butler et al., 2005; Polyakov et al., 2007; Guilbaud et al., 2011;

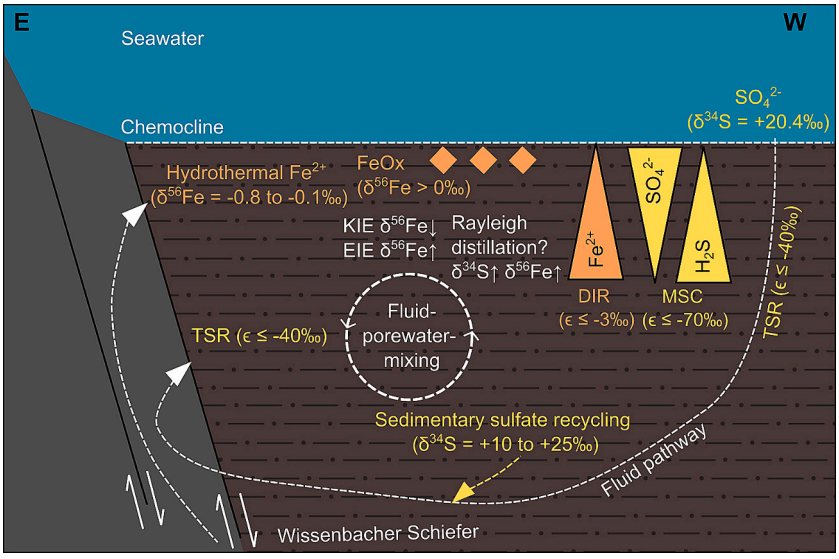

Fig. 8. Plausible sulfur ($\delta^{34}S$) and iron ($\delta^{56}Fe$) isotope systematics in the Rammelsberg system. Yellow features denote reservoirs and processes affecting the sulfur pool. Orange features denote reservoirs and processes affecting the iron pool. FeOx: Fe(III) (oxyhydr)oxides, KIE: Kinetic isotope effect, EIE: Equilibrium isotope effect, DIR: Dissimilatory Fe(III) reduction, MSC: Microbial sulfur cycling, TSR: Thermochemical sulfate reduction. Geological context, isotopic compositions of reservoirs, and fractionation factors (ε) associated with relevant processes were compiled from Anger et al. (1966); Eldridge et al. (1988); Ono, 2008; Sáez et al. (2011); Mansor and Fantle (2019); Hoefs (2021). (For interpretation of the references to colour in this figure legend, the reader is referred to the web version of this article.)

Syverson et al., 2013; Rolison et al., 2018; Mansor and Fantle, 2019), matching our observation.

In summary, either (hydrothermal) pyritization of isotopically distinct precursors or partial equilibration of pyrite with hydrothermal Fe(II), or a combination of both, can explain the observed δ^{56}Fe variability. Thus, our iron isotope data are inconclusive regarding signatures of microbial iron cycling. At the same time, however, they are consistent with the two-step model of early diagenetic microbial pyrite formation and strong secondary isotope exchange during hydrothermal overprint inferred from textural observation and sulfur isotope data.

5.4. Implications for biosignature detection in modern and ancient hydrothermal deposits

Volcanogenic and sediment-hosted massive sulfide deposits commonly show bulk and in-situ $\Delta^{34}S_{pyrite}$ variations of ~30 ‰ (Eldridge et al., 1988, 1993; Taylor, 2004; Present et al., 2017; Lode et al., 2017; Slack et al., 2019; Velasco-Acebes et al., 2019; Nozaki et al., 2020, 2024; Liu et al., 2022). These δ^{34}S signatures are typically texture-specific and interpreted as an early low-δ^{34}S framboid-like pyrite, resulting from MSC, and a late high-δ^{34}S subhedral to euhedral pyrite, precipitated from a hydrothermal sulfur source. Despite sulfur isotope evidence for a minor microbial contribution to pyrite formation in the Rammelsberg deposit and the Wissenbacher Schiefer (Anger et al., 1966; Nielsen, 1985; Eldridge et al., 1988; Large and Walcher, 1999; this study), it cannot be conclusively resolved for most of our sulfur isotope data. Moreover, the similar δ^{56}Fe ranges and distributions between framboid-like and subhedral pyrite did not allow for discrimination between early diagenetic (microbial) versus secondary hydrothermal processes. This suggests that detecting signatures of microbial iron cycling in the hitherto poorly explored δ^{56}Fe record of sediment-hosted massive sulfide deposits may prove challenging in future studies. Instead, our textural, δ^{34}S, Δ^{33}S, and δ^{56}Fe data collectively suggest a strong hydrothermal contribution to pyrite formation. Possible diagnostic signatures of early diagenetic redox cycling were likely erased or altered by secondary hydrothermal processes in most cases (Fig. 8). Thus, our results stress that resolving microbial redox cycling in hydrothermal sulfides is challenging, even in low-temperature systems (130–180 °C) that experienced only greenschist facies metamorphism later in their history.

Despite these challenges, the likely detection of microbial pyrite in the Rammelsberg deposit was possible by reconstructing its diagenetic history using textural observations, stable isotope data, and the specific geological context of our sample. Regardless of an abiogenic or biogenic pyrite origin, δ^{34}S and δ^{56}Fe values consistent with microbial redox cycling were not fully equilibrated with hydrothermal fluids, as observed in previous studies on other localities (e.g., Marin-Carbonne et al., 2020). This highlights that potential biosignatures can survive hydrothermal alteration of the precursor sediment and low-grade post-depositional metamorphism (Ramdohr, 1953; Muchez and Stassen, 2006; Runge et al., 2023a).

The oldest hydrothermal sulfides occur in up to 3.5-billion-year-old (Ga) rocks of the Barberton Greenstone Belt and Pilbara Craton (South Africa and Western Australia, respectively). This includes the Bien Venue Formation and Sulphur Springs Group (both ca. 3.2 Ga) as well as the Dresser Formation (ca. 3.5 Ga), the latter of which hosts some of the oldest well-preserved evidence for life on Earth (Vearncombe et al., 1995; Van Kranendonk et al., 2008; Hofmann, 2011; Duda et al., 2018; Mißbach et al., 2021; Runge et al., 2023a; Weimann et al., 2024; Baumgartner et al., 2024). Notably, these deposits experienced no more than greenschist facies metamorphism (Buick et al., 2002; Kohler and Anheusser, 2002; Terabayashi et al., 2003; Tice et al., 2004), similar to the Rammelsberg deposit (Ramdohr, 1953; Muchez and Stassen, 2006). Hence, our study stresses that Earth's most ancient hydrothermal sulfide systems may still be valuable targets for deciphering past microbial processes by in-situ sulfur and iron isotope analysis.

6. Conclusions

Our integrated textural and secondary ion mass spectrometry stable isotope analysis (δ^{34}S, Δ^{33}S, δ^{56}Fe) of pyrite from the 390 Ma Rammelsberg sediment-hosted sulfide deposit revealed multiple generations of pyrite formation. While all our δ^{34}S and Δ^{33}S compositions are consistent with either hydrothermal or microbial sulfide, the isotopically lightest pyrite ($\delta^{34}S = -15.13$ ‰; framboid-like) is best explained by an early diagenetic (microbial) origin and secondary hydrothermal recrystallization or cementation by sulfide from thermochemical sulfate reduction. This is supported by differences in median δ^{56}Fe between framboid-like and subhedral pyrite, suggesting a variable expression of kinetic and equilibrium effects between earlier and later pyrite. The overall δ^{56}Fe variability in our sample was inconclusive regarding microbial iron cycling but may reflect the pyritization of a diagenetically fractionated iron pool and/or varying degrees of equilibration with hydrothermal Fe(II). In concert, these results imply a sequence from early diagenetic framboid-like pyrite to hydrothermal alteration and subhedral pyrite formation. Our study highlights that detecting signatures of microbial redox cycling in hydrothermal sulfides comes with unique challenges. However, the likely detection of originally microbial pyrite and the incomplete equilibration of stable isotope signatures demonstrates that such signals can be preserved in sediment-hosted massive sulfides, despite pervasive alteration of the precursor sediments by hydrothermal fluids and later greenschist metamorphism. We stress that coupling in-situ sulfur and iron isotope analysis with detailed textural analysis of pyrite is crucial for tracking biogeochemical cycles throughout the geological record, perhaps including some of the oldest rocks on Earth.

CRediT authorship contribution statement

Eric Runge: Writing – review & editing, Writing – original draft, Visualization, Validation, Methodology, Investigation, Formal analysis, Data curation, Conceptualization. **Muammar Mansor:** Writing – review & editing, Supervision, Project administration, Methodology, Conceptualization. **Virgil Pasquier:** Writing – review & editing, Validation, Software, Methodology, Investigation, Formal analysis, Data curation. **Thomas Bovay:** Writing – review & editing, Validation, Methodology, Formal analysis. **Johanna Marin-Carbonne:** Writing – review & editing, Software, Resources, Methodology. **Vanessa Fichtner:** Writing – review & editing, Conceptualization. **Andreas Kappler:** Writing – review & editing, Supervision, Project administration, Funding acquisition. **Jan-Peter Duda:** Writing – review & editing, Supervision, Resources, Project administration, Funding acquisition, Conceptualization.

Declaration of generative AI and AI-assisted technologies in the writing process

During the preparation of this work the authors used Grammarly in order to spell-check the manuscript. After using this tool/service, the authors reviewed and edited the content as needed and take full responsibility for the content of the publication.

Declaration of competing interest

The authors declare that they have no known competing financial interests or personal relationships that could have influenced the work reported in this paper.

Acknowledgments

This study was supported by the DFG (SPP 1833, Emmy Noether Programme; DU 1450/3-2, DU 1450/7-1; JPD, ER; INST 37/1027-1 FUGG; AK) and the German Excellence Strategy of the German

Federal and State Governments (EXC2124, 390838134; Tübingen Structural Microscopy Core Facility; AK, MM). We thank Jeremiah Shuster and Stefan Fischer for their SEM work and Axel Hackmann and Simone Schafflick for their support in sample preparation. Eckart Walcher provided valuable insights into the Wissenbacher Schiefer and the ore genesis in the Rammelsberg deposit. We thank the SwissSIMS team for their help during the analysis and for maintaining the instrument.

Appendix A. Supplementary data

Contains SEM images of SIMS analysis spots and $\delta^{34}S$, $\Delta^{33}S$, and $\delta^{56}Fe$ data reported in this study. Supplementary data to this article can be found online at [https://doi.org/10.1016/j.chemgeo.2025.122885].

Data availability

Data are available in the supplementary materials and through Mendeley data at Doi: 10.17632/8ybcmxdy5c.1.

References

Anger, G., Nielson, H., Puchelt, H., Ricke, W., 1966. Sulfur isotopes in the Rammelsberg ore deposit (Germany). Econ. Geol. 61, 511–536. https://doi.org/10.2113/gsecongeo.61.3.511.

Baumgartner, R.J., Caruso, S., Fiorentini, M.L., Van Kranendonk, M.J., Martin, L., Jeon, H., Pagès, A., Wacey, D., 2020. Sulfidization of 3.48 billion-year-old stromatolites of the Dresser Formation, Pilbara Craton: constraints from in-situ sulfur isotope analysis of pyrite. Chem. Geol. 538, 119488. https://doi.org/10.1016/j.chemgeo.2020.119488.

Baumgartner, R.J., et al., 2022. Exceptional preservation of organic matter and iron-organic colloidal mineralization in hydrothermal black smoker-type sulfide mineralization from the Paleoarchean seafloor. Chem. Geol., 121296 https://doi.org/10.1016/j.chemgeo.2022.121296.

Baumgartner, R.J., Van Kranendonk, M.J., Caruso, S., Campbell, K.A., Dobson, M.J., Teece, B.L., Verrall, M., Homann, M., Lalonde, S., Visscher, P.T., 2024. Pyritic stromatolites from the paleoarchean dresser formation, pilbara craton: resolving biogenicity and hydrothermally influenced ecosystem dynamics. Geobiology 22, e12610. https://doi.org/10.1111/gbi.12610.

Baya, C., et al., 2021. Influence of trace level As or Ni on pyrite formation kinetics at low temperature. Geochim. Cosmochim. Acta 300, 333–353. https://doi.org/10.1016/j.gca.2021.01.042.

Beard, B.L., Johnson, C.M., Cox, L., Sun, H., Nealson, K.H., Aguilar, C., 1999. Iron isotope biosignatures. Science 285, 1889–1892. https://doi.org/10.1126/science.285.5435.1889.

Bendt, G., Saddeler, S., Schulz, S., 2019. Sulfidation of magnetite nanoparticles – following the polysulfide pathway. Eur. J. Inorg. Chem. 602–608. https://doi.org/10.1002/ejic.201801075.

Benning, L.G., Wilkin, R.T., Barnes, H.L., 2000. Reaction pathways in the Fe–S system below 100°C. Chem. Geol. 167, 25–51. https://doi.org/10.1016/S0009-2541(99)00198-9.

Berg, J.S., Duverger, A., Cordier, L., Laberty-Robert, C., Guyot, F., Miot, J., 2020. Rapid pyritization in the presence of a sulfur/sulfate-reducing bacterial consortium. Sci. Rep. 10, 8264. https://doi.org/10.1038/s41598-020-64990-6.

Berner, R.A., 1984. Sedimentary pyrite formation: an update. Geochim. Cosmochim. Acta 48, 605–615. https://doi.org/10.1016/0016-7037(84)90089-9.

Bradley, A.S., Leavitt, W.D., Schmidt, M., Knoll, A.H., Girguis, P.R., Johnston, D.T., 2016. Patterns of sulfur isotope fractionation during microbial sulfate reduction. Geobiology 14, 91–101.

Bronner, R., et al., 2023. Co-reduction of Fe(III) and S^0 drives Fe-S biomineral formation and phosphate mobilisation. Geochem. Perspect. Lett. 24, 27–32. https://doi.org/10.7185/geochemlet.2301.

Buchholz, P., Luppold, F.W., 2008. Litho-und Biostratigrafie des älteren Mitteldevons im Oberharz. Z. Dtsch. Ges. Geowiss. 159, 263–281.

Buick, R., et al., 2002. Geochronology and stratigraphic relationships of the Sulphur Springs Group and Strelley Granite: A temporally distinct igneous province in the Archaean Pilbara Craton, Australia. Precambrian Res., 114, pp. 87–120. https://doi.org/10.1016/S0301-9268(01)00221-2.

Buschendorf, F., Nielsen, H., Puchelt, H., Ricke, W., 1963. Schwefel-Isotopen-Untersuchungen am Pyrit-Sphalerit-Barit-Lager Meggen/Lenne (Deutschland) und an verschiedenen Devon-Evaporiten. Geochim. Cosmochim. Acta 27, 501–523.

Butler, I.B., Böttcher, M.E., Rickard, D., Oldroyd, A., 2004. Sulfur isotope partitioning during experimental formation of pyrite via the polysulfide and hydrogen sulfide pathways: implications for the interpretation of sedimentary and hydrothermal pyrite isotope records. Earth Planet. Sci. Lett. 228, 495–509. https://doi.org/10.1016/j.epsl.2004.10.005.

Butler, I.B., Archer, C., Vance, D., Oldroyd, A., Rickard, D., 2005. Fe isotope fractionation on FeS formation in ambient aqueous solution. Earth Planet. Sci. Lett. 236, 430–442. https://doi.org/10.1016/j.epsl.2005.05.022.

Cai, C., Li, H., Li, K., Wang, D., 2022. Thermochemical sulfate reduction in sedimentary basins and beyond: a review. Chem. Geol. 607, 121018. https://doi.org/10.1016/j.chemgeo.2022.121018.

Canfield, D.E., 2001. Biogeochemistry of sulfur isotopes. In: Valley, J.W., Cole, D.R. (Eds.), Reviews in Mineralogy and Geochemistry, vol. 43, pp. 607–636.

Canfield, D.E., Berner, R.A., 1987. Dissolution and pyritization of magnetite in anoxic marine sediments. Geochim. Cosmochim. Acta 51, 645–659. https://doi.org/10.1016/0198-0254(87)90182-8.

Canfield, D.E., Raiswell, R., Bottrell, S., 1992. The reactivity of sedimentary iron minerals toward sulfide. Am. J. Sci. 292, 659–683.

Canfield, D.E., Thamdrup, B., Fleischer, S., 1998. Isotope fractionation and sulfur metabolism by pure and enrichment cultures of elemental sulfur-disproportionating bacteria. Limnol. Oceanogr. 43, 253–264. https://doi.org/10.4319/lo.1998.43.2.0253.

Chambers, L.A., Trudinger, P.A., Smith, J.W., Burns, M.S., 1975. Fractionation of sulfur isotopes by continuous cultures of *Desulfovibrio desulfuricans*. Can. J. Microbiol. 21, 1602–1607.

Chanda, P., Amenabar, M.J., Boyd, E.S., Beard, B.L., Johnson, C.M., 2021. Stable Fe isotope fractionation during dissimilatory Fe(III) reduction by a thermoacidophile in acidic hydrothermal environments. Geochim. Cosmochim. Acta 292, 427–451. https://doi.org/10.1016/j.gca.2020.09.025.

Chang, J., Li, Y., Lu, H., 2022. The morphological characteristics of authigenic pyrite formed in marine sediments. J. Mar. Sci. Eng. 10, 1533. https://doi.org/10.3390/jmse10101533.

Chever, F., Rouxel, O.J., Croot, P.L., Ponzevera, E., Wuttig, K., Auro, M., 2015. Total dissolvable and dissolved iron isotopes in the water column of the Peru upwelling regime. Geochim. Cosmochim. Acta 162, 66–82. https://doi.org/10.1016/j.gca.2015.04.031.

Crosby, H.A., Johnson, C.M., Roden, E.E., Beard, B.L., 2005. Coupled Fe(II)−Fe(III) electron and atom exchange as a mechanism for Fe isotope fractionation during dissimilatory iron oxide reduction. Environ. Sci. Technol. 39, 6698–6704. https://doi.org/10.1021/es0505346.

Crosby, H.A., Roden, E.E., Johnson, C.M., Beard, B.L., 2007. The mechanisms of iron isotope fractionation produced during dissimilatory Fe(III) reduction by *Shewanella putrefaciens* and *Geobacter sulfurreducens*. Geobiology 5, 169–189. https://doi.org/10.1111/j.1472-4669.2007.00103.x.

Dauphas, N., John, S.G., Rouxel, O., 2017. Iron isotope systematics. Rev. Mineral. Geochem. 82, 415–510. https://doi.org/10.2138/rmg.2017.82.11.

Dauphas, N., Heard, A.W., Rego, E.S., Rouxel, O., Marin-Carbonne, J., Pasquier, V., Bekker, A., Rowley, D., 2024. Past and present dynamics of the iron biogeochemical cycle. In: Treatise in Geochemistry. Elsevier. https://doi.org/10.1016/B978-0-323-99762-1.00059-0.

Decraene, M.-N., Marin-Carbonne, J., Thomazo, C., Olivier, N., Philippot, P., Strauss, H., Deloule, E., 2021. Intense biogeochemical iron cycling revealed in Neoarchean micropyrites from stromatolites. Geochim. Cosmochim. Acta 312, 299–320. https://doi.org/10.1016/j.gca.2021.07.020.

Domingos, J.M., Runge, E., Dreher, C., Chiu, T.-H., Shuster, J., Fischer, S., Kappler, A., Duda, J.-P., Xu, J., Mansor, M., 2023. Inferred pyrite growth via the particle attachment pathway in the presence of trace metals. Geochem. Perspect. Lett. 26, 14–19. https://doi.org/10.7185/geochemlet.2318.

Donald, R., Southam, G., 1999. Low temperature anaerobic bacterial diagenesis of ferrous monosulfide to pyrite. Geochim. Cosmochim. Acta 63, 2019–2023. https://doi.org/10.1016/S0016-7037(99)00140-4.

Drake, H., Whitehouse, M.J., Heim, C., Reiners, P.W., Tillberg, M., Hogmalm, K.J., Dopson, M., Broman, C., Åström, M.E., 2018. Unprecedented ^{34}S-enrichment of pyrite formed following microbial sulfate reduction in fractured crystalline rocks. Geobiology 16, 556–574. https://doi.org/10.1111/gbi.12297.

Duda, J.-P., Van Kranendonk, M.J., Thiel, V., Ionescu, D., Strauss, H., Schäfer, N., Reitner, J., 2016. A rare glimpse of paleoarchean life: Geobiology of an exceptionally preserved microbial mat facies from the 3.4 Ga Strelley Pool Formation, Western Australia. PLoS ONE 11, e0147629. https://doi.org/10.1371/journal.pone.0147629.

Duda, J.-P., Thiel, V., Bauersachs, T., Mißbach, H., Reinhardt, M., Schäfer, N., Van Kranendonk, M.J., Reitner, J., 2018. Ideas and perspectives: hydrothermally driven redistribution and sequestration of early Archaean biomass – the "hydrothermal pump hypothesis". Biogeosciences 15, 1535–1548. https://doi.org/10.5194/bg-15-1535-2018.

Dupeyron, J., Decraene, M.-N., Marin-Carbonne, J., Busigny, V., 2023. Formation pathways of Precambrian sedimentary pyrite: Insights from in situ Fe isotopes. Earth Planet. Sci. Lett. 609, 118070. https://doi.org/10.1016/j.epsl.2023.118070.

Eickmann, B., Thorseth, I.H., Peters, M., Strauss, H., Bröcker, M., Pedersen, R.B., 2014. Barite in hydrothermal environments as a recorder of subseafloor processes: a multiple-isotope study from the Loki's Castle vent field. Geobiology 12, 308–321. https://doi.org/10.1111/gbi.12086.

Eldridge, D.L., Farquhar, J., 2018. Rates and multiple sulfur isotope fractionations associated with the oxidation of sulfide by oxygen in aqueous solution. Geochim. Cosmochim. Acta 237, 240–260. https://doi.org/10.1016/j.gca.2018.06.030.

Eldridge, C.S., Compston, W., Williams, I.S., Both, R.A., Walshe, J.L., Ohmoto, H., 1988. Sulfur isotope variability in sediment-hosted massive sulfide deposits as determined using the ion microprobe SHRIMP. I, An example from the Rammelsberg orebody. Econ. Geol. 83, 443–449. https://doi.org/10.2113/gsecongeo.83.2.443.

Eldridge, C.S., Williams, N., Walshe, J.L., 1993. Sulfur isotope variability in sediment-hosted massive sulfide deposits as determined using the ion microprobe SHRIMP; II, a study of the H.Y.C. Deposit at McArthur River, Northern Territory, Australia. Econ. Geol. 88, 1–26. https://doi.org/10.2113/gsecongeo.88.1.1.

Eldridge, D.L., Guo, W., Farquhar, J., 2016. Theoretical estimates of equilibrium sulfur isotope effects in aqueous sulfur systems: highlighting the role of isomers in the

sulfite and sulfoxylate systems. Geochim. Cosmochim. Acta 195, 171–200. https://doi.org/10.1016/j.gca.2016.09.021.
Eldridge, D.L., Kamyshny, A., Farquhar, J., 2021. Theoretical estimates of equilibrium sulfur isotope effects among aqueous polysulfur and associated compounds with applications to authigenic pyrite formation and hydrothermal disproportionation reactions. Geochim. Cosmochim. Acta 310, 281–319. https://doi.org/10.1016/j.gca.2021.05.051.
England, G.L., Rasmussen, B., Krapez, B., Groves, D.I., 2002. Palaeoenvironmental significance of rounded pyrite in siliciclastic sequences of the late Archaean Witwatersrand Basin: oxygen-deficient atmosphere or hydrothermal alteration? Sedimentology 49, 1133–1156. https://doi.org/10.1046/j.1365-3091.2002.00479.x.
Farquhar, J., Johnston, D.T., Wing, B.A., Habicht, K.S., Canfield, D.E., Airieau, S., Thiemens, M.H., 2003. Multiple sulphur isotopic interpretations of biosynthetic pathways: implications for biological signatures in the sulphur isotope record. Geobiology 1, 27–36. https://doi.org/10.1046/j.1472-4669.2003.00007.x.
Farquhar, J., Johnston, D.T., Wing, B.A., 2007. Implications of conservation of mass effects on mass-dependent isotope fractionations: influence of network structure on sulfur isotope phase space of dissimilatory sulfate reduction. Geochim. Cosmochim. Acta 71, 5862–5875. https://doi.org/10.1016/j.gca.2007.08.028.
Fortney, N.W., He, S., Converse, B.J., Beard, B.L., Johnson, C.M., Boyd, E.S., Roden, E.E., 2016. Microbial Fe(III) oxide reduction potential in chocolate pots hot spring, Yellowstone National Park. Geobiology 14, 255–275. https://doi.org/10.1111/gbi.12173.
Früh-Green, G.L., Kelley, D.S., Lilley, M.D., Cannat, M., Chavagnac, V., Baross, J.A., 2022. Diversity of magmatism, hydrothermal processes and microbial interactions at mid-ocean ridges. Nat. Rev. Earth Environ. 3, 852–871. https://doi.org/10.1038/s43017-022-00364-y.
Gagnevin, D., Boyce, A.J., Barrie, C.D., Menuge, J.F., Blakeman, R.J., 2012. Zn, Fe and S isotope fractionation in a large hydrothermal system. Geochim. Cosmochim. Acta 88, 183–198. https://doi.org/10.1016/j.gca.2012.04.031.
Georgieva, M.N., Little, C.T.S., Maslennikov, V.V., Glover, A.G., Ayupova, N.R., Herrington, R.J., 2021. The history of life at hydrothermal vents. Earth Sci. Rev. 217, 103602. https://doi.org/10.1016/j.earscirev.2021.103602.
Goodfellow, W.D., 1987. Anoxic stratified oceans as a source of sulphur in sediment-hosted stratiform ZnPb deposits (Selwyn Basin, Yukon, Canada). Chem. Geol. 65, 359–382. https://doi.org/10.1016/0168-9622(87)90014-5.
Gorlas, A., et al., 2022. Precipitation of greigite and pyrite induced by thermococcales: an advantage to live in Fe- and S-rich environments? Environ. Microbiol. 1462–2920. https://doi.org/10.1111/1462-2920.15915.
Guilbaud, R., Butler, I.B., Ellam, R.M., 2011. Abiotic pyrite formation produces a large Fe isotope fractionation. Science 332, 1548–1551. https://doi.org/10.1126/science.1202924.
Habicht, K.S., Gade, M., Thamdrup, B., Berg, P., Canfield, D.E., 2002. Calibration of sulfate levels in the Archean Ocean. Science 298, 2372–2374.
Halevy, I., Fike, D.A., Pasquier, V., Bryant, R.N., Wenk, C.B., Turchyn, A.V., Johnston, D. T., Claypool, G.E., 2023. Sedimentary parameters control the sulfur isotope composition of marine pyrite. Science 382, 946–951. https://doi.org/10.1126/science.adh1215.
Hoefs, J., 2021. Stable isotope geochemistry. In: Springer Textbooks in Earth Sciences, Geography and Environment. Springer International Publishing, Cham. https://doi.org/10.1007/978-3-030-77692-3.
Hofmann, A., 2011. Archaean hydrothermal systems in the Barberton Greenstone Belt and their significance as a habitat for early life. In: Golding, S.D., Glikson, M. (Eds.), Earliest Life on Earth: Habitats, Environments and Methods of Detection. Springer Netherlands, Dordrecht, pp. 51–78. https://doi.org/10.1007/978-90-481-8794-2_3.
Huston, D.L., Pehrsson, S., Eglington, B.M., Zaw, K., 2010. The geology and metallogeny of volcanic-hosted massive sulfide deposits: variations through geologic time and with tectonic setting. Econ. Geol. 105, 571–591. https://doi.org/10.2113/gsecongeo.105.3.571.
Johnson, C.M., Beard, B.L., Roden, E.E., 2008. The iron isotope fingerprints of redox and biogeochemical cycling in modern and ancient earth. Annu. Rev. Earth Planet. Sci. 36, 457–493. https://doi.org/10.1146/annurev.earth.36.031207.124139.
Johnson, C., Beard, B., Weyer, S., 2020. Iron geochemistry: an isotopic perspective, 360. Springer International Publishing, Cham. https://doi.org/10.1007/978-3-030-33828-2.
Johnston, D.T., 2005. Multiple sulfur isotope fractionations in biological systems: a case study with sulfate reducers and sulfur disproportionators. Am. J. Sci. 305, 645–660. https://doi.org/10.2475/ajs.305.6-8.645.
Johnston, D.T., Farquhar, J., Canfield, D.E., 2007. Sulfur isotope insights into microbial sulfate reduction: when microbes meet models. Geochim. Cosmochim. Acta 71, 3929–3947. https://doi.org/10.1016/j.gca.2007.05.008.
Jørgensen, B.B., Isaksen, M.F., Jannasch, H.W., 1992. Bacterial sulfate reduction above 100°C in deep-sea hydrothermal vent sediments. Science 258, 1756–1757. https://doi.org/10.1126/science.258.5089.1756.
Jørgensen, B.B., Böttcher, M.E., Lüschen, H., Neretin, L.N., Volkov, I.I., 2004. Anaerobic methane oxidation and a deep H2S sink generate isotopically heavy sulfides in Black Sea sediments. Geochim. Cosmochim. Acta 68, 2095–2118. https://doi.org/10.1016/j.gca.2003.07.017.
Kappler, A., Bryce, C., Mansor, M., Lueder, U., Byrne, J.M., Swanner, E.D., 2021. An evolving view on biogeochemical cycling of iron. Nat. Rev. Microbiol. 19, 360–374. https://doi.org/10.1038/s41579-020-00502-7.
Kashefi, K., Lovley, D.R., 2003. Extending the upper temperature limit for life. Science 301, 934. https://doi.org/10.1126/science.1086823.
Kelley, K.D., Leach, D.L., Johnson, C.A., Clark, J.L., Fayek, M., Slack, J.F., Anderson, V. M., Ayuso, R.A., Ridley, W.I., 2004. Textural, compositional, and sulfur isotope variations of sulfide minerals in the red dog Zn-Pb-Ag deposits, brooks Range, Alaska: implications for ore formation. Econ. Geol. 99, 1509–1532.
Kiyosu, Y., Krouse, H.R., 1990. The role of organic acid in the abiogenic reduction of sulfate and the sulfur isotope effect. Geochem. J. 24, 21–27. https://doi.org/10.2343/geochemj.24.21.
Kohler, E.A., Anheusser, C.R., 2002. Geology and geodynamic setting of Archaean silicic metavolcaniclastic rocks of the Bien Venue Formation, Fig Tree Group, northeast Barberton greenstone belt, South Africa. Precambrian Res. 116, 199–235. https://doi.org/10.1016/S0301-9268(02)00021-9.
Large, D., Walcher, E., 1999. The Rammelsberg massive sulphide Cu-Zn-Pb-Ba-Deposit, Germany: an example of sediment-hosted, massive sulphide mineralisation. Mineral. Deposita 34, 522–538. https://doi.org/10.1007/s001260050218.
Liang, C., Ji, S., Cao, Y., Liu, K., Wu, J., Hao, F., 2024. Characteristics, origins, and significance of pyrites in deep-water shales. Sci. China Earth Sci. 67, 313–342. https://doi.org/10.1007/s11430-022-1200-0.
Liu, K., Huang, F., Gao, S., Zhang, Z., Ren, Y., An, B., 2022. Morphology of framboidal pyrite and its textural evolution: evidence from the Logatchev area, Mid-Atlantic Ridge. Ore Geol. Rev. 141, 104630. https://doi.org/10.1016/j.oregeorev.2021.104630.
Lode, S., Piercey, S.J., Layne, G.D., Piercey, G., Cloutier, J., 2017. Multiple sulphur and lead sources recorded in hydrothermal exhalites associated with the lemarchant volcanogenic massive sulphide deposit, Central Newfoundland, Canada. Mineral. Deposita 52, 105–128. https://doi.org/10.1007/s00126-016-0652-1.
Luther, G.W., 1991. Pyrite synthesis via polysulfide compounds. Geochim. Cosmochim. Acta 55, 2839–2849. https://doi.org/10.1016/0016-7037(91)90449-F.
Lyons, T.W., Gellatly, A.M., McGoldrick, P.J., Kah, L.C., 2006. Proterozoic sedimentary exhalative (SEDEX) deposits and links to evolving global ocean chemistry. In: Evolution of early Earth's Atmosphere, Hydrosphere, and Biosphere - Constraints from Ore Deposits. Geological Society of America. https://doi.org/10.1130/2006.1198(10).
Machel, H.G., Krouse, H.R., Sassen, R., 1995. Products and distinguishing criteria of bacterial and thermochemical sulfate reduction. Appl. Geochem. 10, 373–389. https://doi.org/10.1016/0883-2927(95)00008-8.
Maclean, L.C.W., Tyliszczak, T., Gilbert, P.U.P.A., Zhou, D., Pray, T.J., Onstott, T.C., Southam, G., 2008. A high-resolution chemical and structural study of framboidal pyrite formed within a low-temperature bacterial biofilm. Geobiology 6, 471–480. https://doi.org/10.1111/j.1472-4669.2008.00174.x.
Mansor, M., Fantle, M.S., 2019. A novel framework for interpreting pyrite-based Fe isotope records of the past. Geochim. Cosmochim. Acta 253, 39–62. https://doi.org/10.1016/j.gca.2019.03.017.
Marin-Carbonne, J., Rollion-Bard, C., Luais, B., 2011. In-situ measurements of iron isotopes by SIMS: MC-ICP-MS intercalibration and application to a magnetite crystal from the Gunflint chert. Chem. Geol. 285, 50–61. https://doi.org/10.1016/j.chemgeo.2011.02.019.
Marin-Carbonne, J., Rollion-Bard, C., Bekker, A., Rouxel, O., Agangi, A., Cavalazzi, B., Wohlgemuth-Ueberwasser, C.C., Hofmann, A., McKeegan, K.D., 2014. Coupled Fe and S isotope variations in pyrite nodules from Archean shale. Earth Planet. Sci. Lett. 392, 67–79. https://doi.org/10.1016/j.epsl.2014.02.009.
Marin-Carbonne, J., et al., 2020. In Situ Fe and S isotope analyses in pyrite from the 3.2 Ga Mendon Formation (Barberton Greenstone Belt, South Africa): evidence for early microbial iron reduction. Geobiology 18, 306–325.
Marin-Carbonne, J., et al., 2022. Early precipitated micropyrite in microbialites: a time capsule of microbial sulfur cycling. Geochem. Perspect. Lett. 21, 7–12. https://doi.org/10.7185/geochemlet.2209.
Martin, A.J., Jamieson, J.W., De Ronde, C.E.J., Layne, G.D., Piercey, G., Brandl, P.A., 2023. Constraining temporal variations in metal and sulfur sources using high-resolution mineral-scale analysis of pyrite: evidence from the Brothers volcano, Kermadec arc, New Zealand. Mineral. Deposita 58, 1237–1262. https://doi.org/10.1007/s00126-023-01177-9.
McAnena, A., Severmann, S., Guilbaud, R., Poulton, S.W., 2024. Iron isotope fractionation during sulfide-promoted reductive dissolution of iron (oxyhydr)oxide minerals. Geochim. Cosmochim. Acta 369, 17–34. https://doi.org/10.1016/j.gca.2024.01.032.
Meng, X., Jin, X., Li, X., Chu, F., Zhu, J., Wang, Y., Zhou, P., 2022. Subseafloor mineralization related to the shallow seawater-hydrothermal circulation system in the Longqi hydrothermal field, Southwest Indian Ridge (49.6°E): evidence from in situ trace element and sulfur isotope compositions of pyrite varieties. Ore Geol. Rev. 145, 104914. https://doi.org/10.1016/j.oregeorev.2022.104914.
Mißbach, H., Duda, J.-P., van den Kerkhof, A.M., Lüders, V., Pack, A., Reitner, J., Thiel, V., 2021. Ingredients for microbial life preserved in 3.5 billion-year-old fluid inclusions. Nat. Commun. 12, 1101. https://doi.org/10.1038/s41467-021-21323-z.
Moreno, C., González, F., Sáez, R., 2019. Basin evolution and massive sulfide deposition at rammelsberg (Germany): updating the subsidence analysis. Minerals 9, 45. https://doi.org/10.3390/min9010045.
Moreras-Marti, A., Fox-Powell, M., Cousins, C.R., Macey, M.C., Zerkle, A.L., 2022. Sulfur isotopes as biosignatures for Mars and Europa exploration. J. Geol. Soc. Lond. 179, jgs2021-134. https://doi.org/10.1144/jgs2021-134.
Muchez, P., Stassen, P., 2006. Multiple origin of the 'kniest feeder zone' of the stratiform Zn–Pb–cu ore deposit of Rammelsberg, Germany. Mineral. Deposita 41, 46–51. https://doi.org/10.1007/s00126-005-0039-1.
Muller, É., Philippot, P., Rollion-Bard, C., Cartigny, P., Assayag, N., Marin-Carbonne, J., Mohan, M.R., Sarma, D.S., 2017. Primary sulfur isotope signatures preserved in high-grade Archean barite deposits of the Sargur Group, Dharwar Craton, India. Precambrian Res. 295, 38–47.
Murowchick, J.B., Barnes, H.L., 1987. Effects of temperature and degree of supersaturation on pyrite morphology. Am. Mineral. 72, 1241–1250.

Nie, M., Li, X., Ding, Y., Pan, Y., Cai, Y., Liu, Y., Liu, J., 2023. Effect of stoichiometry on nanomagnetite sulfidation. Environ. Sci. Technol. 57, 3002–3011. https://doi.org/10.1021/acs.est.2c08179.
Nielsen, H., 1985. In: Sulfur isotope ratios in stratabound mineralizations in Central Europe. Geologisches Jahrbuch, Reihe D 70, pp. 225–262.
Nozaki, T., Nagase, T., Ushikubo, T., Shimizu, K., Ishibashi, J., the D/V Chikyu Expedition 909 Scientists, 2020. Microbial sulfate reduction plays an important role at the initial stage of subseafloor sulfide mineralization. Geology 49, 222–227. https://doi.org/10.1130/G47943.1.
Nozaki, T., Nagase, T., Ushikubo, T., Shimizu, K., Komuro, K., 2024. In situ sulfur isotope analysis of pyrite from the Ezuri Kuroko-type volcanogenic massive sulfide deposit, northeastern Japan: contribution of microbial sulfate reduction to initial sulfide mineralization. Resour. Geol. 74, e12328.
Ono, S., 2008. Multiple-sulphur isotope biosignatures. Space Sci. Rev. 135, 203–220. https://doi.org/10.1007/s11214-007-9267-2.
Otake, T., Yamada, R., Suzuki, R., Nakamura, S., Ito, A., Shin, K.-C., Sato, T., 2021. Large Fe isotope fractionations in sulfide ores and ferruginous sedimentary rocks from the Kuroko volcanogenic massive sulfide deposits in the Hokuroku district, Northeast Japan. Geochim. Cosmochim. Acta 295, 49–64. https://doi.org/10.1016/j.gca.2020.12.009.
Paiste, K., Fike, D.A., Kirsimäe, K., Jones, C., Lepland, A., 2022. Testing the global significance of the sulfur isotope record of the ca. 2.0 Ga Zaonega formation: a micro-scale S isotope investigation. Geochim. Cosmochim. Acta 331, 86–104. https://doi.org/10.1016/j.gca.2022.05.021.
Paiste, K., et al., 2024. Sulfur isotopes from the Paleoproterozoic Francevillian Basin record multigenerational pyrite formation, not depositional conditions. Commun. Earth Environ. 5, 328. https://doi.org/10.1038/s43247-024-01498-1.
Pasquier, V., Rego, E.S., Dupeyron, J., Bouvier, A.-S., Bovay, T., Robyr, M., Marin-Carbonne, J., 2024. SIMS iron isotope measurements of the Balmat pyrite reference material: a non-unique δ^{56}Fe signature. Geostand. Geoanal. Res. 12549. https://doi.org/10.1111/ggr.12549.
Paul, D., 1975. Sedimentologische und geologische untersuchungen zur rekonstruktion des ablagerungsraumes vor und nach bildung der rammelsberger Pb-Zn-Lager: Hannover. Geol. Jahrbuch Reihe D 12, 3–93.
Peiffer, S., Behrends, T., Hellige, K., Larese-Casanova, P., Wan, M., Pollok, K., 2015. Pyrite formation and mineral transformation pathways upon sulfidation of ferric hydroxides depend on mineral type and sulfide concentration. Chem. Geol. 400, 44–55. https://doi.org/10.1016/j.chemgeo.2015.01.023.
Picard, A., Gartman, A., Girguis, P.R., 2016. What do we really know about the role of microorganisms in iron sulfide mineral formation? Front. Earth Sci. 4. https://doi.org/10.3389/feart.2016.00068.
Planavsky, N.J., Crowe, S.A., Fakhraee, M., Beaty, B., Reinhard, C.T., Mills, B.J.W., Holstege, C., Konhauser, K.O., 2021. Evolution of the structure and impact of Earth's biosphere. Nat. Rev. Earth Environ. https://doi.org/10.1038/s43017-020-00116-w.
Pokrovski, G.S., Blanchard, M., Saunier, G., Poitrasson, F., 2021. Mechanisms and rates of pyrite formation from hydrothermal fluid revealed by iron isotopes. Geochim. Cosmochim. Acta 304, 281–304. https://doi.org/10.1016/j.gca.2021.03.006.
Polyakov, V.B., Soultanov, D.M., 2011. New data on equilibrium iron isotope fractionation among sulfides: constraints on mechanisms of sulfide formation in hydrothermal and igneous systems. Geochim. Cosmochim. Acta 75, 1957–1974. https://doi.org/10.1016/j.gca.2011.01.019.
Polyakov, V.B., Clayton, R.N., Horita, J., Mineev, S.D., 2007. Equilibrium iron isotope fractionation factors of minerals: reevaluation from the data of nuclear inelastic resonant X-ray scattering and Mössbauer spectroscopy. Geochim. Cosmochim. Acta 71, 3833–3846. https://doi.org/10.1016/j.gca.2007.05.019.
Popa, R., Kinkle, B.K., Badescu, A., 2004. Pyrite framboids as biomarkers for iron-sulfur systems. Geomicrobiol J. 21, 193–206. https://doi.org/10.1080/01490450490275497.
Poulton, S.W., Krom, M.D., Raiswell, R., 2004. A revised scheme for the reactivity of iron (oxyhydr)oxide minerals towards dissolved sulfide. Geochim. Cosmochim. Acta 68, 3703–3715. https://doi.org/10.1016/j.gca.2004.03.012.
Present, T.M., Bergmann, K.D., Myers, C., Slotznick, S.P., Creveling, J.R., Zieg, J., Fischer, W.W., Knoll, A.H., Grotzinger, J.P., 2017. Pyrite-walled tube structures in a mesoproterozoic sediment-hosted metal sulfide deposit. Geol. Soc. Am. Bull. 130, 598–616.
Qian, G., Brugger, J., Skinner, W.M., Chen, G., Pring, A., 2010. An experimental study of the mechanism of the replacement of magnetite by pyrite up to 300°C. Geochim. Cosmochim. Acta 74, 5610–5630. https://doi.org/10.1016/j.gca.2010.06.035.
Qian, G., Brugger, J., Testemale, D., Skinner, W., Pring, A., 2013. Formation of As(II)-pyrite during experimental replacement of magnetite under hydrothermal conditions. Geochim. Cosmochim. Acta 100, 1–10. https://doi.org/10.1016/j.gca.2012.09.034.
Ramdohr, P., 1953. Mineralbestand, Strukturen und Genesis der Rammelsberg-Lagerstätte. Geol. Jahrb. 67, 367–494.
Rasmussen, B., 2000. Filamentous microfossils in a 3,235-million-year-old volcanogenic massive sulphide deposit. Nature 405, 676–679.
Reinhardt, M., et al., 2024. Aspects of the biological carbon cycle in a ca. 3.42-billion-year-old marine ecosystem. Precambrian Res. 402, 107289. https://doi.org/10.1016/j.precamres.2024.107289.
Rickard, D., 1969. The microbiological formation of iron sulphides. Contrib. Geol. 20, 49–66.
Rickard, D.T., 1975. Kinetics and mechanism of pyrite formation at low temperatures. Am. J. Sci. 275, 636–652.
Rickard, D., 1997. Kinetics of pyrite formation by the H2S oxidation of iron (II) monosulfide in aqueous solutions between 25 and 125°C: the rate equation. Geochim. Cosmochim. Acta 61, 115–134. https://doi.org/10.1016/S0016-7037(96)00321-3.
Rickard, D., 2019. How long does it take a pyrite framboid to form? Earth Planet. Sci. Lett. 513, 64–68. https://doi.org/10.1016/j.epsl.2019.02.019.
Rolison, J.M., Stirling, C.H., Middag, R., Gault-Ringold, M., George, E., Rijkenberg, M.J. A., 2018. Iron isotope fractionation during pyrite formation in a sulfidic Precambrian Ocean analogue. Earth Planet. Sci. Lett. 488, 1–13. https://doi.org/10.1016/j.epsl.2018.02.006.
Rouxel, O., Fouquet, Y., Ludden, J.N., 2004. Subsurface processes at the lucky strike hydrothermal field, mid-atlantic ridge: evidence from sulfur, selenium, and iron isotopes. Geochim. Cosmochim. Acta 68, 2295–2311. https://doi.org/10.1016/j.gca.2003.11.029.
Rouxel, O., Shanksiii, W., Bach, W., Edwards, K., 2008. Integrated Fe- and S-isotope study of seafloor hydrothermal vents at East Pacific rise 9–10°N. Chem. Geol. 252, 214–227. https://doi.org/10.1016/j.chemgeo.2008.03.009.
Roy, M., Rouxel, O., Martin, J.B., Cable, J.E., 2012. Iron isotope fractionation in a sulfide-bearing subterranean estuary and its potential influence on oceanic Fe isotope flux. Chem. Geol. v. 300–301, 133–142. https://doi.org/10.1016/j.chemgeo.2012.01.022.
Runge, E.A., Mansor, M., Kappler, A., Duda, J.-P., 2023a. Microbial biosignatures in ancient hydrothermal sulfides. Geobiology 21, 355–377.
Runge, E.A., Mansor, M., Shuster, J., Fischer, S., Liu, Y., Lunter, D.J., Kappler, A., Duda, J.-P., 2023b. Sulfidation of nano-magnetite to pyrite: Implications for interpreting paleoenvironmental proxies and biosignature records in hydrothermal sulfide deposits. Earth Planet. Sci. Lett. 617, 118261. https://doi.org/10.1016/j.epsl.2023.118261.
Runge, E., Mansor, M., Chiu, T.-H., Shuster, J., Fischer, S., Kappler, A., Duda, J.-P., 2024. Hydrothermal sulfidation of biogenic magnetite produces framboid-like pyrite. Commun. Earth Environ. 5, 252.
Sáez, R., Moreno, C., González, F., Almodóvar, G.R., 2011. Black shales and massive sulfide deposits: causal or casual relationships? Insights from Rammelsberg, Tharsis, and Draa Sfar. Mineral. Deposita 46, 585–614. https://doi.org/10.1007/s00126-010-0311-x.
Sansjofre, P., Cartigny, P., Trindade, R.I.F., Nogueira, A.C.R., Agrinier, P., Ader, M., 2016. Multiple sulfur isotope evidence for massive oceanic sulfate depletion in the aftermath of Snowball Earth. Nat. Commun. 7, 12192. https://doi.org/10.1038/ncomms12192.
Sawlowicz, Z., 1993. Pyrite framboids and their development: a new conceptual mechanism. Geol. Rundsch. 82, 148–156. https://doi.org/10.1007/BF00563277.
Schoonen, M.A.A., Barnes, H.L., 1991. Mechanisms of pyrite and marcasite formation from solution: III. Hydrothermal processes. Geochim. Cosmochim. Acta 55, 3491–3504. https://doi.org/10.1016/0016-7037(91)90050-F.
Severmann, S., Johnson, C.M., Beard, B.L., German, C.R., Edmonds, H.N., Chiba, H., Green, D.R.H., 2004. The effect of plume processes on the Fe isotope composition of hydrothermally derived Fe in the deep ocean as inferred from the Rainbow vent site, Mid-Atlantic Ridge, 36°14′N. Earth Planet. Sci. Lett. 225, 63–76. https://doi.org/10.1016/j.epsl.2004.06.001.
Severmann, S., Johnson, C.M., Beard, B.L., McManus, J., 2006. The effect of early diagenesis on the Fe isotope compositions of porewaters and authigenic minerals in continental margin sediments. Geochim. Cosmochim. Acta 70, 2006–2022. https://doi.org/10.1016/j.gca.2006.01.007.
Sim, M.S., Bosak, T., Ono, S., 2011a. Large sulfur isotope fractionation does not require disproportionation. Science 333, 74–77. https://doi.org/10.1126/science.1205103.
Sim, M.S., Ono, S., Donovan, K., Templer, S.P., Bosak, T., 2011b. Effect of electron donors on the fractionation of sulfur isotopes by a marine Desulfovibrio sp. Geochim. Cosmochim. Acta 75, 4244–4259. https://doi.org/10.1016/j.gca.2011.05.021.
Sim, M.S., Woo, D.K., Kim, B., Jeong, H., Joo, Y.J., Hong, Y.W., Choi, J.Y., 2023. What controls the sulfur isotope fractionation during dissimilatory sulfate reduction? ACS Environ. Au 3, 76–86. https://doi.org/10.1021/acsenvironau.2c00059.
Sivan, O., Adler, M., Pearson, A., Gelman, F., Bar-Or, I., John, S.G., Eckert, W., 2011. Geochemical evidence for iron-mediated anaerobic oxidation of methane. Limnol. Oceanogr. 56, 1536–1544.
Slack, J.F., Shanks, W.C., Ridley, W.I., Dusel-Bacon, C., DesOrmeau, J.W., Ramezani, J., Fayek, M., 2019. Extreme sulfur isotope fractionation in the late Devonian Dry Creek volcanogenic massive sulfide deposit, Central Alaska. Chem. Geol. 513, 226–238. https://doi.org/10.1016/j.chemgeo.2019.03.007.
Smrzka, D., Lin, Z., Monien, P., Chen, T., Bach, W., Peckmann, J., Bohrmann, G., 2024. Pyrite-based trace element fingerprints for methane and oil seepage. Geochem. Perspect. Lett. 29, 33–37. https://doi.org/10.7185/geochemlet.2409.
Sperling, H., 1986. das neue lager der blei-zink-lagerstätte rammelsberg: Hannover. Geol. Jahrbuch Reihe D 85, 5–177.
Spinks, S.C., et al., 2021. Carbonate replacement as the principal ore formation process in the proterozoic McArthur River (HYC) sediment-hosted Zn-Pb Deposit, Australia. Econ. Geol. 116, 693–718. https://doi.org/10.5382/econgeo.4793.
Strauss, H., 1997. The isotopic composition of sedimentary sulfur through time. Palaeogeogr. Palaeoclimatol. Palaeoecol. 132, 97–118.
Syverson, D.D., Borrok, D.M., Seyfried, W.E., 2013. Experimental determination of equilibrium Fe isotopic fractionation between pyrite and dissolved Fe under hydrothermal conditions. Geochim. Cosmochim. Acta 122, 170–183. https://doi.org/10.1016/j.gca.2013.08.027.
Taylor, B.E., 2004. Biogenic and thermogenic sulfate reduction in the Sullivan Pb–Zn–Ag deposit, British Columbia (Canada): evidence from micro-isotopic analysis of carbonate and sulfide in bedded ores. Chem. Geol. 204, 215–236. https://doi.org/10.1016/j.chemgeo.2003.11.011.

Terabayashi, M., Masada, Y., Ozawa, H., 2003. Archean Ocean-floor metamorphism in the North Pole area, Pilbara Craton, Western Australia. Precambrian Res. 127, 167–180. https://doi.org/10.1016/S0301-9268(03)00186-4.

Thiel, J., Byrne, J.M., Kappler, A., Schink, B., Pester, M., 2019. Pyrite formation from FeS and H2S is mediated through microbial redox activity. Proc. Natl. Acad. Sci. 116, 6897–6902. https://doi.org/10.1073/pnas.1814412116.

Thomazo, C., et al., 2019. Multiple sulfur isotope signals associated with the late Smithian event and the Smithian/Spathian boundary. Earth Sci. Rev. 195, 96–113. https://doi.org/10.1016/j.earscirev.2018.06.019.

Tice, M.M., Bostick, B.C., Lowe, D.R., 2004. Thermal history of the 3.5–3.2 Ga Onverwacht and Fig Tree Groups, Barberton greenstone belt, South Africa, inferred by Raman microspectroscopy of carbonaceous material. Geology 32, 37. https://doi.org/10.1130/G19915.1.

Toner, B.M., Rouxel, O.J., Santelli, C.M., Bach, W., Edwards, K.J., 2016. Iron transformation pathways and redox micro-environments in seafloor sulfide-mineral deposits: spatially resolved Fe XAS and δ57/54Fe observations. Front. Microbiol. 7. https://doi.org/10.3389/fmicb.2016.00648.

Tornos, F., Peter, J.M., Allen, R., Conde, C., 2015. Controls on the siting and style of volcanogenic massive sulphide deposits. Ore Geol. Rev. 68, 142–163. https://doi.org/10.1016/j.oregeorev.2015.01.003.

Truong, C., Bernard, S., Le Pape, P., Morin, G., Baya, C., Merrot, P., Gorlas, A., Guyot, F., 2023. Production of carbon-containing pyrite spherules induced by hyperthermophilic thermococcales: a biosignature? Front. Microbiol. 14, 1145781. https://doi.org/10.3389/fmicb.2023.1145781.

Truong, C., Bernard, S., Gorlas, A., Guyot, F., 2024. Abiotic syntheses of pyrite: clues to assess the biogenicity of pyrite spherules. Geochem. Perspect. Lett. 32, 27–33. https://doi.org/10.7185/geochemlet.2438.

Van Kranendonk, M., Philippot, P., Lepot, K., Bodorkos, S., Pirajno, F., 2008. Geological setting of Earth's oldest fossils in the ca. 3.5 Ga dresser formation, Pilbara Craton, Western Australia. Precambrian Res. 167, 93–124. https://doi.org/10.1016/j.precamres.2008.07.003.

Vearncombe, S., Barley, M.E., Groves, D.I., McNaughton, N.J., Mikucki, E.J., Vearncombe, J.R., 1995. 3.26 Ga black smoker-type mineralization in the Strelley Belt, Pilbara Craton, Western Australia. J. Geol. Soc. Lond. 152, 587–590. https://doi.org/10.1144/gsjgs.152.4.0587.

Velasco-Acebes, J., Tornos, F., Kidane, A.T., Wiedenbeck, M., Velasco, F., Delgado, A., 2019. Isotope geochemistry tracks the maturation of submarine massive sulfide mounds (Iberian Pyrite Belt). Mineral. Deposita 54, 913–934. https://doi.org/10.1007/s00126-018-0853-x.

Wacey, D., Noffke, N., Cliff, J., Barley, M.E., Farquhar, J., 2015. Micro-scale quadruple sulfur isotope analysis of pyrite from the ~3480Ma dresser formation: new insights into sulfur cycling on the early Earth. Precambrian Res. 258, 24–35. https://doi.org/10.1016/j.precamres.2014.12.012.

Walcher, E.H., 1986. Geologisch-lagerstättenkundliche Untersuchungen am Zeitäquivalent (Lagerhorizont) der Lagerstätte Rammelsberg [PhD thesis]:. Technische Universität Clausthal, p. 84.

Wan, M., Schröder, C., Peiffer, S., 2017. Fe(III):S(-II) concentration ratio controls the pathway and the kinetics of pyrite formation during sulfidation of ferric hydroxides. Geochim. Cosmochim. Acta 217, 334–348. https://doi.org/10.1016/j.gca.2017.08.036.

Wang, Q., Morse, J.W., 1996. Pyrite formation under conditions approximating those in anoxic sediments I. Pathway and morphology. Mar. Chem. 52, 99–121. https://doi.org/10.1016/0304-4203(95)00082-8.

Wang, S., Li, C., Li, B., Dang, Y., Ye, J., Zhu, Z., Zhang, L., Shi, X., 2022. Constraints on fluid evolution and growth processes of black smoker chimneys by pyrite geochemistry: a case study of the Tongguan hydrothermal field, South Mid-Atlantic Ridge. Ore Geol. Rev. 140, 104410. https://doi.org/10.1016/j.oregeorev.2021.104410.

Wang, Q., Wang, J., Wang, X., Kumar, N., Pan, Z., Peiffer, S., Wang, Z., 2023. Transformations of ferrihydrite–extracellular polymeric substance coprecipitates driven by dissolved sulfide: interrelated effects of carbon and sulfur loadings. Environ. Sci. Technol. https://doi.org/10.1021/acs.est.2c06921.

Weimann, L., et al., 2024. Carbonaceous matter in ~ 3.5 Ga black bedded barite from the Dresser Formation (Pilbara Craton, Western Australia) – Insights into organic cycling on the juvenile Earth. Precambrian Res. 403, 107321. https://doi.org/10.1016/j.precamres.2024.107321.

Whitehouse, M.J., 2013. Multiple sulfur isotope determination by SIMS: evaluation of reference sulfides for Δ^{33} S with observations and a case study on the determination of Δ^{36} S. Geostand. Geoanal. Res. 37, 19–33. https://doi.org/10.1111/j.1751-908X.2012.00188.x.

Whitehouse, M.J., Fedo, C.M., 2007. Microscale heterogeneity of Fe isotopes in >3.71 Ga banded iron formation from the Isua Greenstone Belt, southwest Greenland. Geology 35, 719. https://doi.org/10.1130/G23582A.1.

Wilkinson, J.J., 2014. Sediment-hosted zinc–lead mineralization. In: Treatise on Geochemistry. Elsevier, pp. 219–249. https://doi.org/10.1016/B978-0-08-095975-7.01109-8.

Wing, B.A., Halevy, I., 2014. Intracellular metabolite levels shape sulfur isotope fractionation during microbial sulfate respiration. Proc. Natl. Acad. Sci. 111, 18116–18125. https://doi.org/10.1073/pnas.1407502111.

Wu, N., Farquhar, J., Strauss, H., 2014. δ34S and Δ33S records of paleozoic seawater sulfate based on the analysis of carbonate associated sulfate. Earth Planet. Sci. Lett. 399, 44–51. https://doi.org/10.1016/j.epsl.2014.05.004.

Zaback, D.A., Pratt, L.M., Hayes, J.M., 1993. Transport and reduction of sulfate and immobilization of sulfide in marine black shales. Geology 21, 141. https://doi.org/10.1130/0091-7613(1993)021<0141:TAROSA>2.3.CO;2.

Zerkle, A.L., Jones, D.S., Farquhar, J., Macalady, J.L., 2016. Sulfur isotope values in the sulfidic Frasassi cave system, Central Italy: a case study of a chemolithotrophic S-based ecosystem. Geochim. Cosmochim. Acta 173, 373–386. https://doi.org/10.1016/j.gca.2015.10.028.